Space Sci Rev
DOI 10.1007/s11214-014-0114-y

The Wide-Field Imager for Solar Probe Plus (WISPR)

Angelos Vourlidas · Russell A. Howard · Simon P. Plunkett · Clarence M. Korendyke · Arnaud F.R. Thernisien · Dennis Wang · Nathan Rich · Michael T. Carter · Damien H. Chua · Dennis G. Socker · Mark G. Linton · Jeff S. Morrill · Sean Lynch · Adam Thurn · Peter Van Duyne · Robert Hagood · Greg Clifford · Phares J. Grey · Marco Velli · Paulett C. Liewer · Jeffrey R. Hall · Eric M. DeJong · Zoran Mikic · Pierre Rochus · Emanuel Mazy · Volker Bothmer · Jens Rodmann

Received: 20 March 2014 / Accepted: 20 October 2014

Abstract The Wide-field Imager for Solar PRobe Plus (WISPR) is the sole imager aboard the Solar Probe Plus (SPP) mission scheduled for launch in 2018. SPP will be a unique

---

A. Vourlidas (✉)
The Johns Hopkins University Applied Physics Laboratory, Laurel, MD 20732, USA
e-mail: angelos.vourlidas@jhuapl.edu

R.A. Howard · S.P. Plunkett · C.M. Korendyke · A.F.R. Thernisien · D. Wang · N. Rich · M.T. Carter · D.H. Chua · D.G. Socker · M.G. Linton · J.S. Morrill
Space Science Division, Naval Research Laboratory, Washington, DC 20375, USA

S. Lynch · A. Thurn
Naval Center for Space Technology Division, Naval Research Laboratory, Washington, DC 20375, USA

P. Van Duyne
Space Systems Research Corporation, Alexandria, VA 22314, USA

R. Hagood
ATK Space Systems, Beltsville, MD 20705, USA

G. Clifford
Silver Engineering Inc., Melbourne, FL 32904, USA

P.J. Grey
Johns Hopkins University Applied Physics Laboratory, Laurel, MD 20723, USA

M. Velli · P.C. Liewer · J.R. Hall · E.M. DeJong
Jet Propulsion Laboratory, Pasadena, CA 91109, USA

Z. Mikic
Predictive Sciences Inc., San Diego, CA 92121, USA

P. Rochus · E. Mazy
Centre Spatial de Liege, Université de Liège, Liege, Belgium

V. Bothmer · J. Rodmann
Institute of Astrophysics, University of Göttingen, Göttingen, Germany

mission designed to orbit as close as 7 million km (9.86 solar radii) from Sun center. WISPR employs a 95° radial by 58° transverse field of view to image the fine-scale structure of the solar corona, derive the 3D structure of the large-scale corona, and determine whether a dust-free zone exists near the Sun. WISPR is the smallest heliospheric imager to date yet it comprises two nested wide-field telescopes with large-format (2 K × 2 K) APS CMOS detectors to optimize the performance for their respective fields of view and to minimize the risk of dust damage, which may be considerable close to the Sun. The WISPR electronics are very flexible allowing the collection of individual images at cadences up to 1 second at perihelion or the summing of multiple images to increase the signal-to-noise when the spacecraft is further from the Sun. The dependency of the Thomson scattering emission of the corona on the imaging geometry dictates that WISPR will be very sensitive to the emission from plasma close to the spacecraft in contrast to the situation for imaging from Earth orbit. WISPR will be the first 'local' imager providing a crucial link between the large-scale corona and the *in-situ* measurements.

Keywords Solar probe plus · Heliospheric imager · Solar corona · Solar wind · Imaging · Thomson scattering

1 Introduction

The solar wind, the constant outflow of plasma and magnetic field from the Sun's outer layer, the solar corona, was one of the first scientific discoveries of the space era (Parker 1958; Snyder et al. 1963). Its basic properties are well understood around the Earth and, to a lesser degree, in the inner heliosphere thanks to *in-situ* measurements by a large number of solar probes over the years. Unfortunately, the solar wind undergoes significant evolution by the time it reaches the probes and little can be learned about its origins, even at 0.3 AU, as was found by the Helios mission, the closest manmade probes to the Sun to date. All we know with certainty is that the wind originates in the inner solar corona, within the first few solar radii above the solar surface. This region can only be studied with remote sensing imaging and spectroscopic observations, which provide only large-scale information on the density and temperature of the corona and infrequent and restricted (in height) information on the magnetic field (e.g., Cargill 2009 and references therein). As a result, fundamental questions about the physical processes behind the generation and evolution of the solar wind remain open. For example, we do not know what drives the fine scale structure of the wind, how the wind is heated and energized or how it interacts with transient structures such as Coronal Mass Ejections (CMEs) and energetic particles. Clearly, the best way to answer these questions is by inserting a probe directly into the region where the solar wind is born.

1.1 The Solar Probe Plus (SPP) Mission

The Solar Probe Plus (SPP) mission is the most ambitious robotic mission to be implemented by NASA. SPP will fly to within 8.86 solar radii (R_s) above the solar surface making it mankind's first object to enter a star's atmosphere. This is not the only unique aspect of the SPP mission. It will obtain its first observations from 35 R_s, already uncharted territory, within just three months from launch. The 7-year prime phase of the mission includes not just one but three close perihelion passages at 9.86 R_s from the center of the Sun. The probe will swing from 0.25 AU, the start of the observing period, to perihelion in less than five days, enabling observations from rapidly varying heliocentric distances and viewpoints. Its

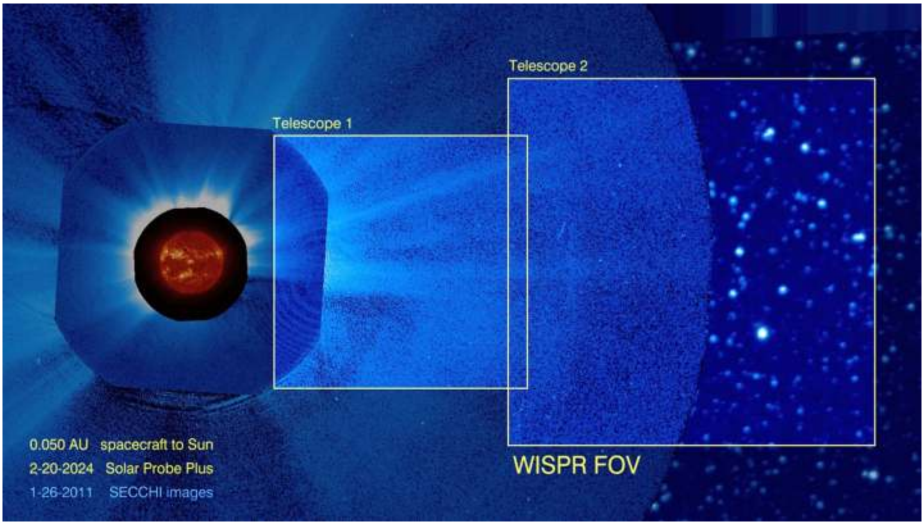

Fig. 1 An approximation of the coronal scene from WISPR. The *yellow boxes* represent the WISPR FOVs at closest perihelia (9.86 R_S) projected onto a combined SECCHI HI and COR2 image. The spatial resolution of WISPR will be about 4× higher than this image (36 arcsec/pix)

orbit will, at times, bring SPP to within a few million km from Mercury, Venus, and probably sungrazer comets. The spacecraft carries three instruments for *in-situ* measurements of particles and fields: the Electromagnetic Fields Investigation (FIELDS; Bale et al. 2014); the Solar Wind Electrons, Alphas, and Protons (SWEAP; Kasper et al. 2014); the Integrated Science Investigation of the Sun Energetic Particle Instruments (ISIS-EPI; McComas et al. 2014). The fourth instrument is the Wide-field Imager for Solar PRobe Plus (WISPR), a heliospheric imager to provide the large-scale context of the structures encountered by the *in-situ* instruments, which we proceed to describe next. More details about the mission design, science objectives and implementation can be found in Fox et al. (2014).

1.2 WISPR Science Background

WISPR is designed, developed and will be operated by the Solar & Heliospheric Physics Branch at the Naval Research Laboratory (NRL). As the only imaging instrument onboard SPP, the WISPR design is guided by two overarching objectives: (1) WISPR should provide the crucial link between the *in-situ* SPP observations and the large scale structure of the corona that is needed to address SPP science, and (2) WISPR should enhance the scientific return of the mission with trailblazing observations of two-dimensional electron density power spectra, interplanetary dust, and sungrazing comets.

WISPR will provide continuous synoptic observations of the inner heliosphere, imaging both the quasi-steady flow and transient disturbances in the solar wind by observing visible sunlight scattered by electrons in the solar wind. Its wide field of view (FOV) will encompass both the inner corona and the plasma in the vicinity of the spacecraft. The WISPR FOV is centered on the ecliptic plane but it is offset from the Sun, and covers a range of elongation angles from 13.5° to 108° with a spatial resolution of 6.4 arcmin (Fig. 1). Table 1 compares the WISPR FOV and resolution at different locations in the SPP orbit with those of current coronal imagers, using 1 AU equivalent quantities (AU_{eq}) to provide a common

Table 1 Comparison of WISPR capabilities to other coronagraphs and imagers

Telescope	Heliocentric Distance (AU)	FOV (R_s, AU_{eq})	Spatial Resolution (arcsec AU_{eq})	Cadence (min)
WISPR	0.25	9.5–83	94	60
	0.1	4.0–41	26	7
	0.044	2.2–20	17	0.05
SoloHI	0.28	5.1–47	25	5
LASCO/C2	1	2.2–6	24	24
SECCHI/COR2	1	2.5–15	30	15
SECCHI/HI1	1	15–90	108	40
SECCHI/HI2	1	74–337	250	120
SMEI	1	74–>337	1440	102

comparison baseline. The numbers refer to objects far from the telescopes. Obviously, the effective resolution for near-field objects will be better as long as those objects are resolved. WISPR's perihelion FOV extends both closer and further from the Sun than the Sun-Earth Connection Coronal and Heliospheric Investigation (SECCHI; Howard et al. 2008) COR2 coronagraph, at about twice the spatial resolution. It includes the Alfvén point, which is expected to lie between 10–30 R_s based on theoretical considerations (see DeForest et al. 2014 and references therein) and is likely never below 5.5 R_s (Sheeley and Wang 2002). Such a wide FOV and high resolution is vital to the success of the SPP mission. Our studies of coronal structure with STEREO and SOHO have shown that there is abundant structure at the resolution limits of those instruments, both in streamers and in CMEs. An instrument unable to resolve these structures would only provide the large-scale context for *in-situ* measurements, a limiting role discussed in the Solar Probe STDT report.[1] The WISPR science program extends beyond that to the study of the substructures of streamer current sheets and CMEs, and to the study of turbulence and shocks as discussed in detail in the next section.

The high-resolution observations will image both co-rotating and transient structures (e.g., CMEs, jets, and plumes in coronal holes) as these structures propagate through the inner corona and ultimately pass over the SPP spacecraft. The rapidly changing FOV will enable detailed tomographic reconstructions of the large and small-scale structure of the background corona. Thus, WISPR will provide both broad and detailed context for interpreting the *in-situ* SPP measurements. Note that WISPR's nominal resolution of 17 arcsec (AU_{eq}) at closest perihelion is a lower limit. Structures approaching the spacecraft will be imaged at much higher resolution. This provides the second major rationale for designing WISPR with such high resolution.

To take full advantage of the high resolution, WISPR is mounted on the forward, ram-side of the spacecraft. The solar wind structures observed by WISPR move radially outward at speeds equal to or exceeding the orbital speed of SPP at perihelion (∼200 km/s). The ram-side mounted WISPR instrument will therefore image structures prior to their *in-situ* measurement, with increasing resolution, as they rise up from the Sun towards SPP. This allows WISPR to point close to the solar disk and simultaneously image these local structures. The combination of WISPR's high resolution and ram-side mounting allow us to image and study dynamical processes which evolve as the SPP spacecraft approaches and then flies

---

[1] Available at http://solarprobe.jhuapl.edu/mission/docs/SolarProbe_STDT2008.pdf.

Fig. 2 LOS depth of the Thomson scattering emission during a minimum perihelion SPP orbit. The colors/numbers corresponds to three points in the orbit. The contours mark the 5 %, 50 % (*dotted*), and 95 % of the integrated emission along each LOS from 14° to 180° elongation

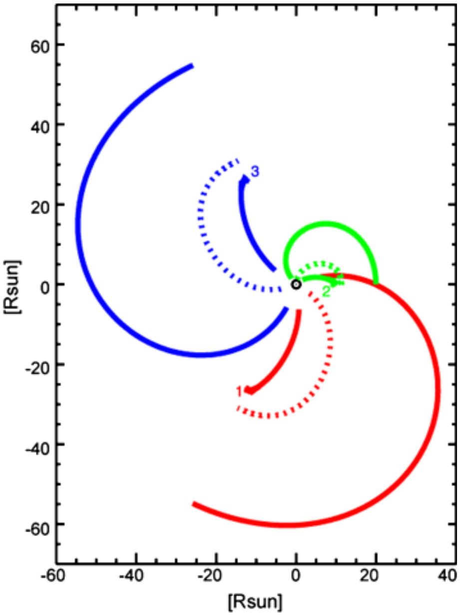

through them, enhancing WISPR's capabilities to support the *in-situ* measurements of both static and dynamical structures.

WISPR will observe the Thomson-scattered light from the solar wind electrons. This scattering process has a sensitivity dependence on the geometry between the Sun, observer and scattering electron. Vourlidas and Howard (2006) have shown that the observing geometry must be taken into account for the proper interpretation of coronagraph and heliospheric imager observations. They introduced the concept of the Thomson surface, which denotes the location of maximum scattering efficiency. Solar wind features at progressively large angular distances from the Thomson surface scatter less than features close to the surface. Because the Thomson surface varies with the Sun-observer distance, it is especially important to understand its effects on the WISPR science analysis. The mission design of the SPP is highly unusual for an imaging instrument due to the rapidly changing orbit and the very close perihelia.

An important consequence of Thomson scattering effect is that the locus of maximum scattering passes through the spacecraft. This means that at the elongation angle of 90°, WISPR becomes an '*in-situ* imager'. This effect was first noted in the Helios analysis of the 90° photometer, which detected an increase in the intensity whenever a CME crossed the spacecraft (Jackson and Leinert 1985). These effects are shown in Fig. 2 for three locations during an orbit at closest perihelion. WISPR is located on the ram-side and we plot the full 180° longitudinal scan, rather than the 90° WIRSP FOV, for completeness. Each color denotes a different part of the orbit and the numbers mark the location of the S/C at that moment. The three contours in each color mark, in increasing distance from the S/C, the 5 %, 50 %, and 95 % of the cumulative brightness along a given elongation (or LOS). At the start of the observing period (marked by '1'), plasma as far as 40 R_s from the spacecraft contributes to the emission. But at perihelion ('2'), only emission within 10 R_s is important. Also, the 50 % emission is almost independent of the elongation while the LOS extends further for elongation >90°. These plots show that the forward quadrant is well observed by the instrument and thus will detect the CMEs, shocks, plasma sheets, that the S/C will then pass through. These plots show that considerable part of the emission at large elongations comes from structures near the S/C (50 % curves). At the same time, the SNR drops quickly with increasing heliocentric distances leading to longer integration times (>60 min, Table 2). Therefore, imaging at large elongations provides less useful tomographic information. More details on the Thomson scattering effects and their implications on Solar Orbiter and SPP missions will be discussed in Vourlidas et al. (2015).

1.3 WISPR Science Objectives and Requirements

WISPR will likely be our only chance to see the fine scales of the solar corona without the complications induced by the intervening interplanetary dust and will create important science synergies with the Solar Orbiter and Bepi-Colombo missions. The WISPR observations will be critical for the science undertaken by the SPP *in-situ* instruments. SPP will undergo numerous perihelion passages at different heliocentric distances. For WISPR, these orbital variations imply both a changing FOV, in terms of heliospheric coverage, and varying spatial resolution in the sky plane (Table 1).

Within these considerations, we designed the WISPR science investigation to address all three Level-1 (L-1) science objectives of the SPP mission. We derive the science requirements, which in turn drive the instrument design (Sect. 3), by posing specific questions under each of the Level-1 objective. The objectives are discussed in detail in Fox et al. (2014) but we repeat them here for completeness.

L-1 Objective: Determine the structure and dynamics of the magnetic fields at the sources of the fast and slow solar wind.

Science Question 1: *'How does the magnetic field in the solar wind source regions connect to the photosphere and the heliosphere?'*

Studies of streamers are the primary means for addressing this question, as they are relatively steady structures from which the slow solar wind is thought to emanate. *In-situ* observations of the magnetic fields and plasma properties of these structures along the 1D spacecraft trajectory will be combined with remote white light observations by WISPR. Previous *in-situ* observations from outside 0.3 AU have been extrapolated back to the Sun, indicating that the slow wind may originate in these streamers and the closed magnetic fields below them (e.g. Gosling et al. 1981). This conclusion has been supported by remote sensing of the slow wind, for example by interplanetary scintillation measurements from Voyager 2 (Woo and Martin 1997) and via SOHO Ultraviolet Coronal Spectrometer (UVCS; Kohl et al. 1995) Doppler measurements combined with context images from the Large Angle and Spectrometric Coronagraph (LASCO; Brueckner 1995) coronagraphs (Habbal et al. 1997). SPP will for the first time allow us to definitively test this inference. WISPR will image streamers as SPP approaches them, giving a highly accurate measure of when and through which part (i.e., edge, center) the spacecraft flies. The *in-situ* observations will then measure the plasma properties and the magnetic field in and around that streamer, telling us what the solar wind characteristics are in the streamer, and how they vary across the streamer.

WISPR will address fundamental questions about the structure of streamers: Are streamers the folds of a single current sheet encompassing the Sun or are there multiple current sheets which create multiple streamers? Does this structure change from solar minimum to solar maximum? What is the internal structure of streamers? High-resolution WISPR observations on par with those of the LASCO and SECCHI coronagraphs will put the *in-situ*

Table 2 WISPR Science Requirements Traceability Matrix

Science Objective	**1. Trace the flow of energy that heats and accelerates the solar corona and solar wind.**			**2. Determine the structure and dynamics of the plasma and magnetic fields at the sources of the solar wind.**			
Science Question #	**1**	**2**		**3**	**4**		**5**
Science Measurement Objective	Velocity and brightness evolution of small scale features in coronal holes and streamers	Location, morphology of the stream interface boundaries, and wave turbulence		Map morphology of coronal structure to SPP orbit	Velocity and brightness evolution of small scale features in coronal holes and streamers		Velocity, acceleration and mass density of evolving structures
Science Measurements	H-t and mass measurements of solar wind features	H-t and mass measurements of solar wind features	Power spectra of density fluctuations at different heliocentric distances	Images of coronal and heliospheric solar wind structures in visible	H-t and mass measurements of solar wind features	Density power spectra at various heliocentric distances	H-t and mass measurements of solar wind features
Observation Requirements							
Scene Radial Coverage	14°- 90°		14° - 20°	14°- 90°		14° - 20°	14°- 90°
Scene Transverse Coverage	25°- 55°		12°	25°- 55°		12°	25°- 55°
Solar Latitude Coverage	-45° to +40°[5]		-25° to +15°	-45° to +40°[5]		-25° to +15°	-45° to +40°[5]
Image Spatial Resolution (arcmin)	≤ 6.4[1,2,3] to ≤ 25.6[4b]		≤ 6.4	≤ 6.4[1,2,3] to ≤ 25.6[4b]		≤ 6.4	≤ 6.4[1,2,3] to ≤ 25.6[4b]
Photometric Sensitivity (Signal-to-Noise Ratio)	≥ 20[1,2], ≥ 5 [3,4]		≥ 20	≥ 20[1,2], ≥ 5 [3,4]		≥ 20	≥ 20[1,2], ≥ 5 [3,4]
Cadence (min)	≤ 40[1,2,3] ≤ 80[4]	≤ 2.5[1a] to ≤ 16.5 [4a] ≤ 4.5[1b] to ≤ 40[4b] ≤ 9.0[1c] to ≤ 80[4c]	≤ 4 sec	≤ 40[1,2,3] ≤ 80[4]	≤ 2.5[1a] to ≤ 16.5[4a] ≤ 4.5[1b] to ≤ 40[4b] ≤ 9.0[1c] to ≤ 80[4c]	≤ 4 sec	≤ 18[1,2] ≤ 40[3], ≤ 80[4]
Baseline Mission Observing Period (days)	240		15	240		15	240

Spacecraft Distance from Sun / Elongation:

[1] 0.046-0.07 AU

[1a] 14°-39° for 0.046-0.07 AU

[1b] 39°-69° for 0.046-0.07 AU

[1c] 69°-90° for 0.046-0.07 AU

[2] 0.07-0.11 AU

[3] 0.11 - 0.174 AU

[3a] 14°-39° for 0.11-0.174 AU

[4] 0.174- 0.25 AU

[4a] 14°-39° for 0.174-0.25 AU

[4b] 39°-65° for 0.174-0.25 AU

[4c] 65°-90° for 0.174-0.25 AU

[5] at 14°

[*] 10 min image sequences per hr

Table 2 (*Continued*)

Science Objective	**3. Explore mechanisms that accelerate and transport energetic particles.**		**G1. Explore dusty plasma phenomena in the near-Sun environment and their influence on the solar wind and energetic particle formation.**	
Science Question #	**6**	**7**	**8**	**9**
Science Measurement Objective	Location, morphology and speed of shocks near the Sun	Morphology, velocity, acceleration of CMEs and shocks out to SPP orbit	F-corona brightness, morphology and variability as a function of heliocentric distance	Location, morphology of CMEs and coronal evolution along SPP orbit
Science Measurements	High cadence height-time plots and density measurements of CME fronts	High cadence height-time plots and density measurements of CME fronts	Images of F-corona during the orbit	Images and height plots of the corona ahead of SPP passage
Observation Requirements				
Scene Radial Coverage	14°-60°	14°- 90°	14°- 90°	14°- 90°
Scene Transverse Coverage	25°- 55°	25°- 55°	25°- 55°	
Solar Latitude Coverage	-45° to +40°^{5}	-45° to +40°^{5}	-45° to +40°^{5}	
Image Spatial Resolution (arcmin)	≤ 6.4	≤ 6.4	≤ 6.4^{1,2,3} to ≤ 25.6^{4b}	
Photometric Sensitivity (Signal-to-Noise Ratio)	≥ 20^{1,2}, ≥ 5^{3,4}	≥ 20^{1,2}, ≥ 5^{3,4}	≥ 20^{1,2}, ≥ 5^{3,4}	
Cadence (min)	≤ 5	≤ 5^{1a,1b} ≤ 10^{1c}	≤ 80	≤ 40^{1,2,3} ≤ 80^{4}
Baseline Mission Observing Period (days)	240	240	240	

Spacecraft Distance from Sun / Elongation:

[1] 0.046-0.07 AU

[1a] 14°-39° for 0.046-0.07 AU

[1b] 39°-69° for 0.046-0.07 AU

[1c] 69°-90° for 0.046-0.07 AU

[2] 0.07-0.11 AU

[3] 0.11 - 0.174 AU

[3a] 14°-39° for 0.11-0.174 AU

[4] 0.174- 0.25 AU

[4a] 14°-39° for 0.174-0.25 AU

[4b] 39°-65° for 0.174-0.25 AU

[4c] 65°-90° for 0.174-0.25 AU

[5] at 14°

[*] 10 min image sequences per hr

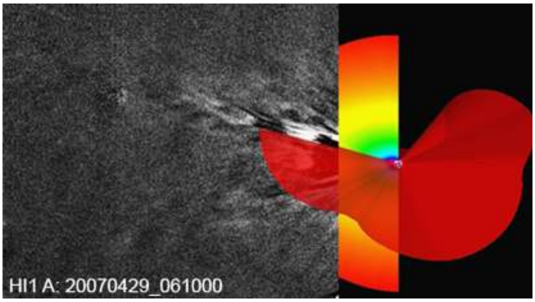

Fig. 3 Comparison of the SECCHI/HI observation of solar wind structures (image) to the heliospheric current sheet (*red surface*) predicted by an MHD model. The meridional slice is the model solar wind velocity (Vourlidas and Riley 2007)

measurements into context. The current coronagraphs observe streamers globally but are unable to measure their 3D structure at resolutions better than 14° (the rate of solar rotation from 1 AU). In contrast, the SPP orbits result in up to 10× faster sweeps around the Sun thus enabling streamer 3D tomographic reconstructions from the WISPR images with spatial resolutions of $\sim 1^\circ$. These reconstructions will allow us to investigate the structures that comprise the heliospheric plasma sheet (HPS) and to study the relation of the HPS to the heliospheric current sheet (HCS), while the SPP *in-situ* magnetic field measurements will determine the presence or absence of current sheets inside streamers. WISPR will image the extension of streamer structures far into the heliosphere and compare their measured location and densities to *in-situ* measurements and coronal models. The SECCHI/HI observations have shown that this is possible. In Fig. 3, taken from Vourlidas and Riley (2007), the location of the HCS, based on an MHD simulation, is projected onto a 2-hour SECCHI/HI running difference image showing quiescent solar wind structures. The figure shows that the largest intensity, therefore density, variability corresponds to locations nearest the HCS. These measurements can identify the sources of the solar wind structures when compared with *in-situ* abundance measurements from SPP, Solar Orbiter, and Earth-orbiting spacecraft.

WISPR will have much better sensitivity and spatial resolution than any other heliospheric imager to date (Table 1). Thus, WISPR images will trace the HPS boundaries, their evolution and their relation relative to the HCS in much greater detail than possible with STEREO. When combined with the in-situ observations from the SPP and other missions (e.g. Solar Orbiter), the WISPR observations will provide strong constraints on the origin and evolution of the solar wind plasma in the heliosphere.

Science Question 2: *'How do the observed structures in the corona evolve into the solar wind?'*

As discussed above, streamers are expected to be the source of the slow solar wind. How they provide this slow wind, however, has not yet been proven, though a number of models of slow solar wind acceleration have been proposed. For example, the models and simulations presented by Einaudi et al. (1999, 2001) show that the slow solar wind can be accelerated in streamers via coupling to the fast solar wind on either side of the streamer current sheet. Tearing modes and Kelvin-Helmholtz modes in the streamer create islands, which are then accelerated by the nearby fast wind (see, e.g., Rappazzo et al. 2005). Antiochos et al. (2007), on the other hand, suggest that the slow solar wind may be accelerated by continuous small-scale reconnection events, which occur between closed and open magnetic fields at the boundaries of coronal holes. WISPR will look for signatures of these mechanisms by

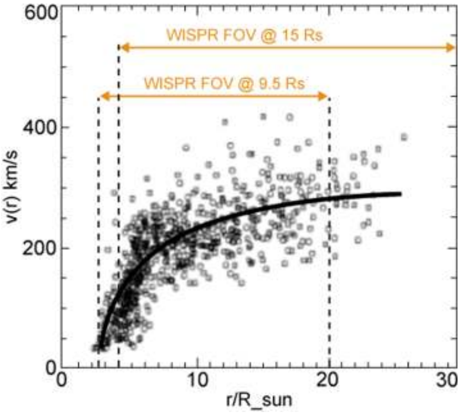

Fig. 4 LASCO speed measurements of streamer blobs. The WISPR fields of view for two perihelia are also shown (modified from Fig. 6, Sheeley et al. 1997)

observing and characterizing structures, which are ejected into the solar wind from streamer current sheets.

White-light imaging with the LASCO coronagraphs has revealed a variety of such dynamical phenomena within the HPS in the outer corona, including plasma blobs that are ejected continually from the cusps of streamers (Sheeley et al. 1997; Wang et al. 1999b; Wang and Sheeley 2006), ray-like structures pervading the streamer belt (Thernisien and Howard 2006), and swarms of small-scale inflows (Wang et al. 1999a; Sheeley and Wang 2001) that occur during times of high solar activity (Fig. 4). The helmet streamers in which these structures are created comprise open field lines lying over closed magnetic loops. Reconnection between open and closed magnetic field lines (Antiochos et al. 2007; interchange reconnection: Crooker et al. 2004; Zurbuchen et al. 2002), between closed magnetic fields lines (generating helical fields) and between open field lines of opposite polarities (Einaudi et al. 1999; Wang et al. 2007; Linton et al. 2009) have all been invoked as the different mechanisms which could trigger the formation and release of such streamer blobs. In addition to serving as a potential source of the slow solar wind, these reconnection processes have a bearing on questions as diverse as the formation and evolution of the HPS/HCS, the heliospheric magnetic flux budget, the solar-cycle evolution of the coronal field, and the rigid rotation of coronal holes. To investigate these phenomena and to test slow solar wind models, we need detailed velocity profiles using high cadence WISPR measurements of streamer outflows, correlated with the *in-situ* measurements. WISPR observations are essential for studying reconnection in the high corona by providing the 3D location and morphology of streamer ejections and measurements of their evolution before the SPP *in-situ* payload intercepts them.

To study the details of these small-scale transients, we need high-resolution observations, as these transients commonly take up only a few pixels in current LASCO and SECCHI coronagraph observations (Sheeley et al. 2008; Rouillard et al. 2008, 2009). WISPR is designed with a 6.4 arcmin resolution so that it can image and trace the streamer blobs, within its FOV, to large heights and with a resolution equivalent to or better than that of the LASCO or SECCHI coronagraphs. The increased resolution and sensitivity of WISPR due to the much smaller contribution of the F-corona brightness (Sect. 1.4) will reduce the scatter in the outer velocity measurements. With the combined WISPR and *in-situ* measurements, we will determine how the slow solar wind densities and speeds vary across the streamer and how that depends on the current sheet structure.

WISPR's wide FOV enables the measurement of the true velocity and acceleration profiles of the transient slow solar wind flows and determine accurately the mass flux contribution of blobs and other ejections to the solar wind. This will provide, for the first time, quantitative tests of the various theoretical models, which explain the origin of the slow solar wind. We will be able to determine if the slow wind is accelerated by viscous coupling to the fast wind just outside the streamer, if it is self-accelerated by turbulence and reconnection within the streamer or if it is accelerated by reconnection in the corona at the boundary between the streamers and coronal holes.

The determination of the local structure of the solar wind as it correlates with the streamer observations is only the first step in understanding the full solar wind geometry. These measurements must then be combined with high-resolution tomographic reconstructions of the transient features, which originate in streamers. This will vastly improve our ability to determine the location, size and propagation direction of these streamer transients. By following the evolution of these transients, we will be able to determine the 3D flows and mass fluxes around streamers and the degree to which these flows are non-radial below the sonic point. Combining these WISPR remote observations with the *in-situ* observations will give us the exciting new capability to reconstruct a significant part of the slow solar wind outflow, providing new insights into the structure of the corona and key inputs for models of coronal fields and solar wind acceleration.

In-situ observations reveal significant fine-scale structure within the fast solar wind which led Feldman et al. (1996) to surmise that these structures are remnants of reconnection events back in the solar corona (e.g., jets, spicules). However, the origin of these fast solar wind structures is unknown because line-of-sight effects and the reduced density within coronal holes hinder the imaging of the fine scale structures from 1 AU, especially for equatorial coronal holes. The proximity of the SPP orbit to the solar corona essentially removes the effects of the F-corona and reduces the number of overlapping structures along the line of sight (LOS) (Sect. 1.4). It provides a unique opportunity to detect and image the faint plasma within coronal holes. WISPR will be able to image this plasma from both equatorial and polar coronal holes up to a heliolatitude of $\sim 40^\circ$ or higher depending on the solar B angle. WISPR will detect the plumes with higher contrast and spatial resolution than has ever been possible. It will measure the plume/interplume density variations and determine the presence of fine scale structure within coronal holes, thus allowing precise measurements of the contribution of plumes and interplume regions to the observed fast wind mass flux. WISPR will be able to image the fast wind for the first time and track such blobs, if they exist, within polar plumes. WISPR will provide these crucial observations over a significant part of the solar cycle. Hence, we will obtain the first detailed measurements of the fast wind acceleration profile over large areas of the corona and, with the addition of the SPP *in-situ* data, provide important constraints for testing theories of fast solar wind acceleration. Together with the slow solar wind observations discussed above, these studies will form comprehensive sets of observations, which will substantially improve our understanding of the sources of the slow and fast solar wind. These measurements will be invaluable as initial condition inputs to the real-time large-scale heliospheric models such as ENLIL and will lead to improved forecasting for space weather conditions at Earth and other planets.

On larger scales, the solar wind flow is disrupted by CMEs. WISPR will contribute to CME studies in two ways. First, the high-resolution WISPR tomographic images will allow us to recreate the 3D structure within CMEs. Second, when combined with *in-situ* measurements of magnetic field and plasma properties, the WISPR observations will allow us to determine the physical state of the ejected CME plasma (thermal, magnetic and kinetic) right at the initial boundary of most CME propagation models (e.g., ENLIL) which will greatly enhance their performance and improve forecasting capabilities. In addition, most

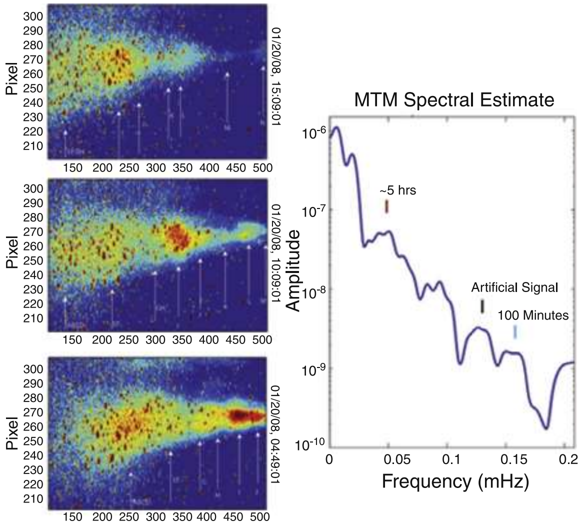

Fig. 5 Periodicities in the solar wind density derive from SECCHI/HI observations. *Left*: Tracing of individual density blobs within a streamer from 15 to 60 R_S. *Right*: The derived periodicities of 5 h (see Viall et al. 2010 for details)

CMEs as observed by current coronagraphs show significant small-scale structure: knots, arches, and even kinks. Currently, only the 3D morphology of the larger structures (e.g., CME outer envelope) can be modeled with SECCHI (Thernisien et al. 2009). WISPR will address this problem with finer scale tomographic reconstructions of CME substructures as SPP passes near or through them.

Science Question 3: *'Is the source of the solar wind steady or intermittent?'*

Various *in-situ* studies have suggested that the inner heliosphere is filled with a network of entangled magnetic flux tubes and that the flux tubes are fossil structures that originate at the solar surface (e.g., Zaqarshvili et al. 2014; Borovsky et al. 2008). The tube walls are associated with large changes in the ion entropy density and the alpha-to-proton ratio. The median size of the flux tubes at 1 AU is 4.4×10^5 km (Borovsky 2006; Borovsky et al. 2008). The magnetic flux in the tubes at 1 AU corresponds to the magnetic flux in field concentrations in the photospheric magnetic carpet. Using 11 years (1995–2005) of solar wind observations from the Wind spacecraft, Viall et al. (2009) showed that periodic proton density structures occurred at particular radial length scales more often than others. An analysis of the alpha to proton solar wind abundance ratio variations strongly suggests that these periodic solar wind density structures originate in the solar corona. Some recent models of abundance variations predict that they are set in the chromosphere (Laming 2009). Because the observed emission is related to the number of electrons along the LOS, intensity variations provide a direct measure of solar wind density variations, which can be compared to Earth-based interplanetary scintillation or SPP *in-situ* measurements. Viall et al. (2010) have identified specific periodicities by following individual blobs of <1200 Mm size through the SECCHI/HI FOV (Fig. 5). The minimum size that could be measured is determined by the cadence and exposure times of the instrument (40 min and 30 min, respectively for HI-1). Our analysis of density data from the SECCHI/HI suggests that we can obtain measures of the fine-scale solar wind variability directly from the WISPR images down to length scales of $\sim$11 Mm at closest perihelion. This estimate is scaled from the results in Viall et al. (2010) using the expected cadence for WISPR (4 s).

L-1 Objective: Trace the flow of energy that heats the solar corona and accelerates the solar wind.

Science Question 4: *'How is energy from the lower solar atmosphere transferred to, and dissipated in, the corona?'*

While the answers to these questions require detailed *in-situ* observations of the plasma and magnetic field in the inner corona, the imaging observations by WISPR can provide essential information to assist the interpretation of the *in-situ* data. There is the possibility that small-scale reconnection heats and accelerates the solar wind. If such reconnection is an important contributor to solar wind heating, then *in-situ* evidence of such events, such as abrupt velocity and magnetic field changes (Gosling et al. 2007) and energetic particles should be quite common. However, tracing their origins (lower atmosphere or the outer corona) using extreme ultraviolet (EUV) or white light imagers on distant platforms (such as SDO or Solar Orbiter) will be difficult due to the small spatial scales involved. By providing high resolution and high dynamic range imaging on the ram-side, WISPR will observe the intermittent solar wind, which is intercepted later by the SPP *in-situ* instruments. Subsequent joint in-situ/imaging analysis on the ground will clarify which, if any, of the observed outflow structures are results of reconnection. The WISPR images can then be compared to coronagraph and EUV imaging from other spacecraft to allow tracing of such features lower in the solar atmosphere.

Science Question 5: *'How do the processes in the corona affect the properties of the solar wind in the heliosphere?'*

While the slow wind appears to originate in streamers, the fast wind originates in the open magnetic fields of coronal holes. The Helios observations revealed that the latitudinal/longitudinal edges of the high-speed solar wind streams from coronal holes are very sharp (Schwenn 1978), with gradients of 100 km/s/deg near 0.3 AU. The sharp edges are less apparent in the Ulysses and near-Earth data perhaps due to interplanetary dispersion on the trailing edges (the fastest plasma runs away from the slower plasma immediately behind it) and because of the change in profile on the leading edges. In contrast to Helios observations, the Wang and Sheeley (1990) numerical model of the solar corona, which relates the expansion of magnetic flux tubes to the speed of the solar wind by assuming that the slow solar wind originates on the boundary of coronal holes, suggests that the latitudinal/longitudinal edges of streams near the Sun are broad regions with gradients of 20 km/s/deg.

WISPR observations will be able to clarify this debate, as it will image the change from low to high-density plasma that marks the transition from high to low speed solar wind. High-resolution white-light images by WISPR will be obtained inside 0.25 AU where, according to Parker spiral theory, the interface between fast and slow solar wind streams will be viewed edge-on. The boundary will appear as a brightness gradient, steepening slowly with increasing heliocentric distance. WISPR images will measure the thickness of the brightness gradient directly and, by tracking its co-rotation over several days, will determine its 3D topology and temporal evolution. Additionally WISPR will pass through the stream interfaces near 10 R_S and *in-situ* observations of the boundary thickness will be compared with white-light observations.

Turbulence is another way the corona affects the solar wind properties. Turbulent cascade, widely accepted as a mechanism for the generation of ion-cyclotron waves, has good theoretical and observational support (Hollweg 2008). However, the solar wind, and consequently its turbulence levels, evolves as the wind propagates away from the Sun, thus

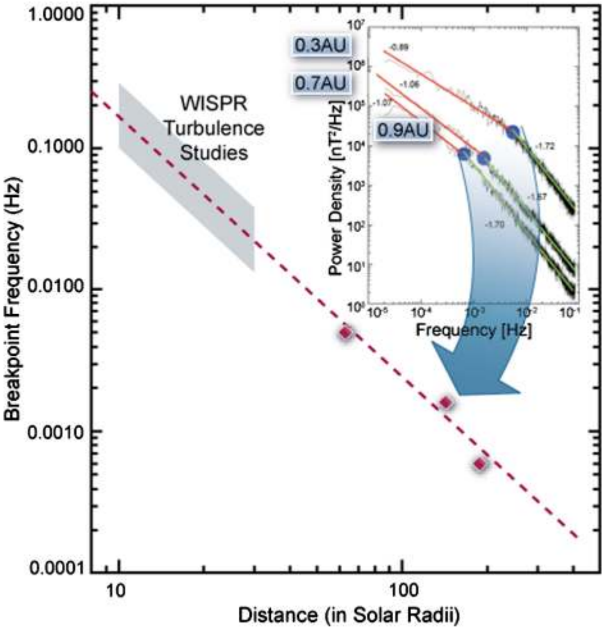

Fig. 6 Estimation of the breakpoint frequency between injection and inertial scales as a function of heliocentric distance based on Helios observations. The simple fit to the three points shows a breakpoint frequency at ∼0.2 Hz at 9.5 R_S, easily accessible by WISPR. *Inset*: The magnetic field spectra used for the breakpoints (Bruno and Carbone 2005)

confusing or diluting signatures of the low corona acceleration processes and of the original wave spectrum. Energy is injected at low frequencies varying from days to months and cascades with a Kolmogorov power spectrum of $f^{-5/3}$. Helios observations have shown that the breakpoint between the inertial and injection scales moves to higher frequencies closer to the Sun but the injection power spectrum maintains the f^{-1} spectrum (Fig. 6). The source of the f^{-1} spectrum is still under debate. Matthaeus and Goldstein (1986) have suggested that it originates from reconnection events in the corona and hence indicates the influence of reconnection in coronal heating. These results are based on solar wind velocity and magnetic field fluctuations. The density fluctuations are harder to interpret. At 1 AU, there is evidence of both turbulence and coherent structures contributing to the observed fluctuations (Viall et al. 2009). To separate them and trace their origins, two-dimensional imaging observations are required. *In-situ* density spectra exhibit f^{-1} and $f^{-5/3}$ spectra (Marsch and Tu 1990) in close correspondence to magnetic field spectra, but they also exhibit $1/f^2$ spectra.

We have only a basic idea of whether this behavior persists closer to the Sun. The main information is provided by density power spectra using interstellar scintillation (e.g., Coles and Harmon 1989) but the relation of the density fluctuations to ion-cyclotron waves is unclear and radio observations near the Sun are rare due to the lack of suitable radio sources and dedicated solar radio instruments. Recently, Bemborad et al. (2008) obtained remote imaging spectra with $1/f$ and $1/f^2$ behavior in the Lyα line using SOHO/UVCS observations. However, the long integration times of 300 s, required to obtain the necessary sensitivity, restricted their study to low frequencies away from the spectral breakpoint. Such studies are further restricted by line-of-sight effects and uncertainties in the origin of the Lyα emission. However, they demonstrated the power of remote imaging by simultaneously obtaining spectra over a variety of longitudes, latitudes and heliocentric distances.

The SPP orbit offers many advantages for the pursuit of such measurements with WISPR based on our experience with the SECCHI/HI performance on solar wind structures. First, the proximity of SPP to the coronal structures allows much higher contrast observations with higher cadence than is possible from 1 AU. Second, the spectral breakpoint between injection and inertial scales is expected to drift from 100 s at 40 R_s down to 5 s at 9.5 R_s based on a simple extrapolation of the Helios measurements (Fig. 6). Both of these time-scales are easily within the WISPR capabilities. We have designed a specific WISPR observing program for this case. For example, prior to each solar encounter, we will use synoptic images from WISPR or other coronagraphs to predict when SPP will cross a solar wind structure of interest (e.g., an HPS boundary or a fast stream interface). For a specified time interval during the SPP perihelion (currently 10 min every hour), WISPR will obtain images over a restricted FOV around the region of interest with extremely high cadence (up to 1 s). A power spectrum of the density fluctuations can then be constructed with variable cadences for direct comparison to similar spectra obtained by the FIELDS instruments on SPP. WISPR will provide density power spectra at or below the spectral break between inertial and injection scales, even at the nearest perihelion approach. WISPR will provide many simultaneous spectra for different coronal structures and will monitor their evolution. When combined with the tomographic information from the synoptic images, the WISPR turbulence program will be a major enhancement to the turbulence measurements from the SPP in-situ instruments resulting in a much more robust understanding of the near-Sun turbulence.

L-1 Objective: Explore the mechanisms that accelerate and transport energetic particles.

Science Question 6: *'What are the roles of shocks, reconnections, waves, and turbulence in the acceleration of energetic particles?'*

CME-driven shocks play a central role in determining the energetic particle populations in the heliosphere and in driving geospace storms. They are known to accelerate solar energetic particles (SEPs) to high energies (e.g., Reames 1999; Kahler 2001), even GeV energies (Bieber et al. 2004) during the so-called gradual SEP events. Fermi acceleration is the likely acceleration mechanism for quasi-parallel shocks while gradient-drift acceleration operates at quasi-perpendicular shocks (e.g., Lee 2000). The geometry of the shock seems to play a further role in the observed variability of the spectral characteristics and composition of SEPs (Tylka 2005). The shock compression ratio determines the power law index of the SEP spectrum under some simplifying assumptions such as equilibrium conditions. It appears that the particle kinetic energy might be a fairly significant percentage of the CME kinetic energy (Mewaldt et al. 2005). Many of these shock-related parameters (geometry, compression ratio, speed) are available or can be deduced from *in-situ* measurements at 1 AU. None, however, is actually measured in the low corona where the highest energy particles originate ($\leq$10 R_s, Tylka 2005). Moreover, the large scatter in the correlation between CME speeds and SEP peak intensities suggests a complex interplay among the CME speed, the acceleration mechanism(s) and the ambient environment.

Some works have focused on the role of the variations of the environment through which the CME shocks and particles propagate (Gopalswamy et al. 2004; Kahler and Vourlidas 2005, 2013). The results indicate that SEP-rich CMEs tend to occur during periods of enhanced activity signifying the presence of elevated levels of seed particles. But the coronagraphic observations also show that SEP-rich CMEs tend to have much brighter fronts than

SEP-poor events. Since bright emission in a coronagraph image may imply a large extent along the LOS, the latter finding suggests that SEP-rich CMEs either attain larger longitudinal and latitudinal extents than SEP-poor CMEs or achieve higher compression ratios. Therefore, the height of formation of the shock, the 3D extent of the CME, and the monitoring of the activity levels (via CMEs, and jets) are necessary observations for a better understanding of the generation and propagation of SEPs.

WISPR will provide these crucial observations for SPP. The telescope will image CMEs and their associated shocks at the coronal heights where the particles originate ($\leq 10\ \mathrm{R_s}$) with high spatial and temporal resolution to resolve the locations of the CME-driven shocks, for all SPP perihelion distances (Table 1). Previous work has shown that CME-driven shocks can be easily detected in coronagraphs (Vourlidas and Ontiveros 2009) and that several physical parameters, such as density compression ratio, speed, and even upstream magnetic field, can be derived. With its higher spatial and sensitivity performance, WISPR will readily observe and characterize the evolution of even the fastest shocks. For example, the synoptic cadence of 5–10 min within 15 $\mathrm{R_s}$ (Table 2) will allow 13–26 observations of a 2000 km/s CME in the WISPR FOV providing detailed information on the evolution of the associated shock.

Science Question 7: *'How are the energetic particles transported radially across magnetic field lines from the corona to the heliosphere?'*

To address this question it is important to characterize accurately the spatial extent of shocks. WISPR will be able to observe the shocks as they expand towards SPP. These observations will monitor the kinematic evolution and the interactions of the shock with the ambient environment providing crucial information for interpreting the *in-situ* observations of the same shock. The WISPR inner FOV extends below 10 $\mathrm{R_s}$ for all heliocentric distances during the science-observing window, and therefore will be able to contribute to the SEP analysis for the entirety of the SPP science operations. WISPR will be able to observe shocks and CMEs as they go over the Solar Orbiter and other inner heliospheric probes that may be operating at the time. The multipoint observations will be used to reconstruct the 3-D structure of CMEs and their associated shocks. Alternatively, the shocks can be localized with the help of type-II radio observations from FIELDS, and the corresponding instruments on Solar Orbiter and STEREO. The rapid image cadence of WISPR ensures that we will record several images of the shock and associated driver before the increased cosmic ray flux due to the accompanying SEPs raises the background noise levels too high for reliable imaging.

1.4 Unique WISPR Science

Besides the WISPR contributions to the SPP Level-1 science objectives, the unique orbit and imaging capabilities of the instrument offer additional science opportunities, which can add considerably to the scientific return of the mission without adding cost or other resources. Therefore, the WISPR team has defined two additional science question goals:

Science Question 8: *'What is the dust environment in the inner heliosphere?'*

The visible emission at 1 AU, from heights above 4 $\mathrm{R_s}$, is dominated by scattering from interplanetary dust, the F-corona. It is a nuisance for coronal studies in the visible as it obscures the signal from CMEs and coronal streamers. Accurate removal of the F-corona is essential for the derivation of coronal density structure (e.g., Hayes et al. 2001) but the current F-coronal models are unreliable, as LASCO/C3 observations have shown. The failure of the models stems from our incomplete understanding of the physical properties and distribution of the dust in the inner heliosphere. Most of what we know comes from coronagraph and eclipse observations from Earth and the *in-situ* and photometric observations from the Helios mission in the 1970's (Leinert et al. 1998).

The F-corona brightness results from the line-of-sight integral of the scattering from 1–100 μm dust particles. These particles undergo efficient forward scattering at small angles. Hence dust located in the region about halfway between the Sun and the observer generates most of the F-corona brightness at small elongations (Mann et al. 2004) resulting in the very stable F-corona emission observed by LASCO. This complicates the inversion of the brightness observations and leads to unreliable determinations of the structure and density distribution of the near-Sun dust and its interplay with planets. For example, the existence of a dust-free zone in the inner corona ($<4\ R_s$) due to sublimation, predicted by Russell (1929), has never been proven experimentally and there is only a marginal detection of a planetary dust ring from Helios observations in the Venus orbit, similar to that seen at Earth's orbit (Leinert and Moster 2007; Jones et al. 2013). Such shortcomings have significant impact on our understanding of dust-plasma interactions and the interpretation of the evolution of circumstellar dust rings and planet formation.

WISPR will revolutionize the remote sensing study of the F-corona by going much closer to the Sun and with much higher sensitivity, spatial resolution and spatial coverage compared to the Helios photometers. Thanks to 18 years of LASCO/C3 observations, we have developed robust data analysis techniques to achieve F-corona model subtractions with accurate photometry. The same techniques are used for the removal of the F-corona from the SECCHI/HI images and the upcoming SoloHI instrument on the Solar Orbiter mission.

With WISPR we will extract quantitative measurements and record the first F-corona images from locations within 0.3 AU. During the perihelion pass, the region of dust contributing to the scattering will move closer to the Sun contributing to an increase in the brightness (due to the increased density of dust) until eventually it must start to roll over close to the Sun and finally disappear at the dust-free zone (Fig. 7). The high orbital velocities during the perihelion passages will result in brightness measurements of the F-corona from a multitude of vantage points relative to the dust cloud thus allowing us to derive much more accurate measurements of the dust density distribution within 0.3 AU. Thanks to the reduced line-of-sight effect, WISPR will be able to detect and measure the boundaries of the dust-free region and possibly verify the existence of dust enhancements in the orbits of Venus and Mercury.

Another unique science opportunity is the search for planetoids within the Mercury orbit. A dynamically stable region interior to Mercury's orbit is predicted to contain a population of small, asteroid like bodies called Vulcanoids from the early solar system and may be the source of impacts onto Mercury. Searches for the existence of Vulcanoids have not been successful. Durda et al. (2000), Merline (2008), and Steffl et al. (2013) have used LASCO, Messenger and SECCHI observations to search for Vulcanoid objects and have put upper limits on the number of objects above certain sizes. While asteroids have been detected within the Vulcanoid region (0.08–0.2 AU), none were Vulcanoids. With WISPR, we will be able to extend these searches to fainter objects and place new constraints on the formation and evolution of objects in this region.

Science Question 9: *'What is the nature of dust–plasma interactions and how does dust modify the spacecraft environment close to the Sun?'*

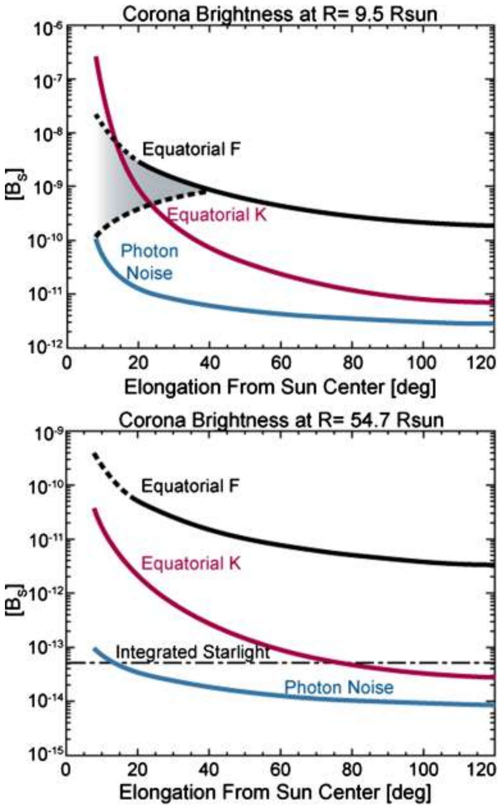

Fig. 7 The predicted coronal brightness from WISPR at altitudes of 9.5 and 54.7 R_S for the equatorial F and K coronae. The photon noise was calculated assuming an exposure time of 1 s for the 9.5 R_S case and 30 min for the 54.7 R_S case. The plots show that WISPR will produce very high SNR images of the solar corona over the instrument FOV

As discussed by Mann et al. (2004), forward scattering washes out the small-scale structure of the corona as well as any information on short-term variability within 0.3 AU from the Sun. Thus, we have no knowledge of the effects of CMEs or sungrazer comets on the dust dynamics near the Sun. WISPR will obtain the first reliable measurements of the F-corona brightness gradient within the first few degrees from the Sun and will observe the evolution of sungrazer (and other comet types) tails within its large FOV.

LASCO observations show that sun-grazing comets occur on average every 2–3 days and their brightness peaks at 10–14 R_s (Knight et al. 2010), right in the middle of the WISPR FOV during close perihelia. Although it is clear they do not survive their perihelion, the actual distance at and process through which their nucleus is disrupted remain unresolved. Most of the sungrazers dim below detection at around 7 R_s and may be completely destroyed by 3 R_s, as a handful of UVCS observations suggest (e.g., Bemborad et al. 2005). Furthermore, Kimura et al. (2002) have suggested that sungrazers should exhibit a second brightness peak at 4–6 R_s due to the sublimation of crystalline and amorphous pyroxenes. WISPR will have the sensitivity, spatial coverage, and cadence to resolve these issues albeit based on a smaller sample of comets than LASCO or SECCHI due to the SPP orbit and operational restrictions.

These comets deposit dust into the near-Sun environment but because of their highly inclined orbits, the dust from their tails must leave the ecliptic quickly. Mann et al. (2004) reached the conclusion that the sun-grazer contribution to the near-Sun dust is negligible but their estimates were based on mass and size distributions derived from SOHO measurements at 1 AU (Sekanina 2001). The actual dust flux and size distribution are unknown and analysis of the WISPR observations is required to determine accurately the contribution of sun-grazer comets to the dust environment.

As discussed above, current F-coronal models are unreliable close to the Sun, but the F-corona brightness must start to roll over, perhaps inside 0.1 AU, due to the increased radiation pressure, evaporation, and Lorentz forces acting on the particles. This effect will be readily detectable by WISPR and will further enhance the quality of the coronal imaging (Fig. 7). Additionally, the radial distances where these processes act on is a function of the particular chemical composition of the species (Mann et al. 2004). So the combination of the WISPR observations with modeling of the dust composition should allow the estimation of the size distribution of the dust in the inner heliosphere. The improvement in the clarity, sensitivity and spatial resolution of the F-corona images combined with the repeated passages over a large part of the cycle will provide the first opportunity to study the short-term (days to years) evolution of the dust and investigate whether CMEs interact in any significant way with the interplanetary dust and whether we can use this interaction to probe the CME magnetic fields, as suggested by Ragot and Kahler (2003).

1.5 Instrument Performance Requirements

The science requirements discussed above drive the instrument performance requirements and define the basic observing sequences. This flow, called the Science Requirements Traceability Matrix (SRTM), is usually presented in table form. In Table 2, we provide an abbreviated version of the SRTM as it stands at the time of the mission Preliminary Design Review (PDR) in January 2014. The top row (in blue) presents the overarching science objectives of the mission, followed by the science questions that WISPR will address via the measurement objectives in the third row.

The types of WISPR measurements (row 4) are typical data products of coronagraphs and heliospheric imagers and should be familiar to most researchers. The density power spectra are a novelty for WISPR (and for the SoloHI instrument on Solar Orbiter). Although such analysis can be employed with the existing imagers and coronagraphs (see discussion under ‘Science Question 5’), it is restricted by the instrument cadences and requires special observing campaigns. In contrast, density power spectra are an integral part of the WISPR observing program (‘wave turbulence’) and drive some of the instrument design, i.e. maximum cadence, readout modes, etc. This measurement type was not envisioned in the STDT report as the report was compiled before the performance of the HI instruments demonstrated the potential of spatially-resolved density power spectra in solar wind physics (Viall et al. 2010). The WISPR team considers the ‘wave turbulence’ program as the key link between the SPP imaging and *in-situ* science with the potential to enhance the scientific return of the mission beyond what was envisioned in the STDT report.

Continuing with the explanation of the SRTM, rows 6–11 present the design requirements for WISPR. These requirements may evolve slightly by the time of the Critical Design Review (CDR; currently planned for December, 2014), as the instrument and spacecraft designs are finalized. However, a few of these requirements, FOV (14°–90°), inner FOV cutoff (14°), spatial resolution (6.4 arcmin), photometric sensitivity (20), and synoptic cadence (16.5 min), are Level-1 requirements and hence are fixed. The ranges in the transverse and equivalent solar latitude coverage reflect the trapezoidal shape of the WISPR FOV (Fig. 1).

An important message in this table is the effect of the varying heliocentric distance and sharp gradients in coronal brightness on the operation of the instrument. The former has never been an issue for previous imaging payloads at an approximately constant 1 AU distance from the Sun. For WISPR, however, the rapidly changing distance and small aperture

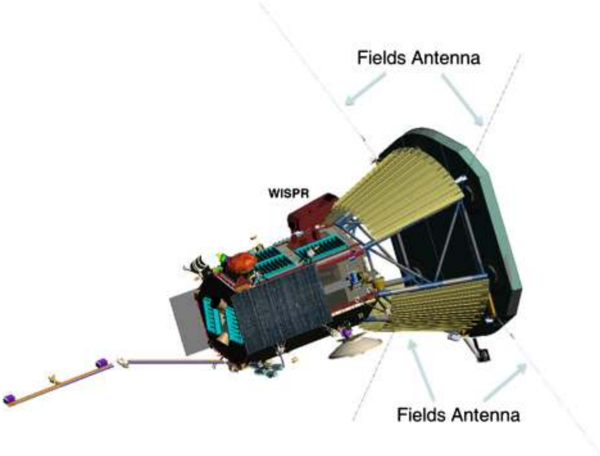

Fig. 8 WISPR Spacecraft Accommodation. The telescope is located on the ram side of the spacecraft, imaging the corona from behind the SPP heat shield through the FIELDS antennas (also shown)

sizes dictated by the mission profile require flexibility in the image acquisition modes and expected sensitivity. This flexibility is expressed in the SRTM with the dependence of the spatial resolution, signal-to-noise ratio, and particularly cadence, on heliocentric distance and solar elongation (rows 9–11). Another point is that most of the programs will run for the duration of the science observing window in each orbit (0.25 AU to 0.046 AU and back to 0.25 AU), with the exception of the wave turbulence program, which is executed during perihelion only (within 0.07 AU) where the spatial resolution and throughput are optimal.

2 WISPR Overview

2.1 Design Philosophy

The WISPR design draws its heritage from the SECCHI heliospheric imagers aboard the Solar Terrestrial Earth Relations Observatory (STEREO; Kaiser et al. 2008) mission and from the SoloHI imager (Howard et al. 2013) under development for ESA's Solar Orbiter mission scheduled for launch in 2017 (Müller et al. 2013). In fact, SoloHI provides many of the design elements and subsystems for adaptation into the WISPR design.

The WISPR instrument is being designed to live within a challenging set of science requirements and resource constraints. In order to achieve the necessary science, WISPR needs to take rapid sequences of images with highly variable signal content across an almost 90° FOV. To achieve this, WISPR uses a combination of baffle systems to greatly reduce incoming stray light, two optical systems to cover the large scene with uniform sensitivity, a novel low-powered radiation-hardened Active Pixel Sensor (APS) detector for each telescope, and an electronics chain with enough bandwidth to process images from both detectors and throttle the data down to meet spacecraft data transfer limits. The electronics and software are designed to meet the science requirements based on the conditions and environments predicted from 0.25 to 0.046 AU, while still allowing the flexibility to adapt to circumstances and observations beyond those requirements.

To optimize the science return of the mission, WISPR is located on the ram-side of the SPP spacecraft viewing the coronal structures to be encountered by the *in-situ* instrumentation (Fig. 8). This is also the reason that the radial FOV extends to 90 degrees elongation. This accommodation may expose the instrument to higher dust flux, during perihelion, than

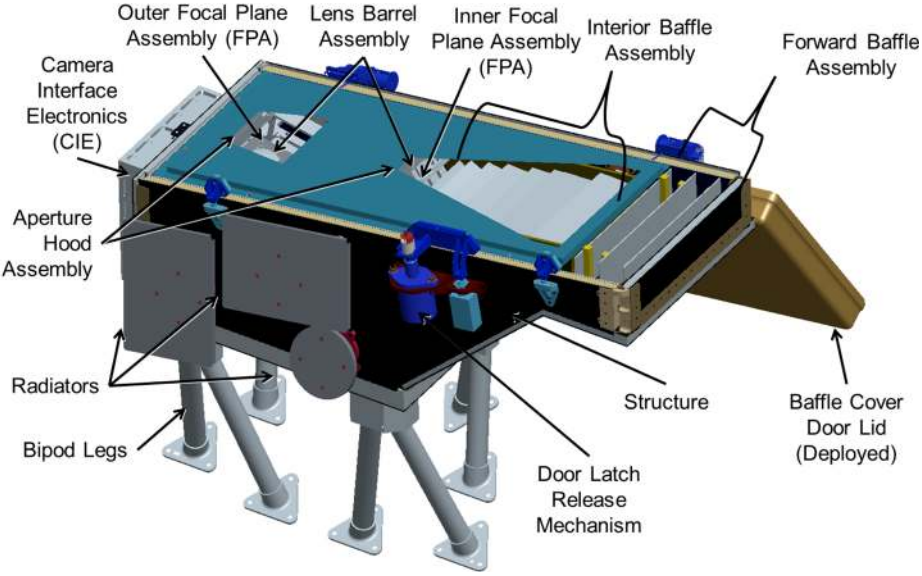

Fig. 9 The WISPR Instrument Module (WIM) and its subassemblies. Two telescopes cover the WISPR FOV: the Inner and Outer telescope. Three baffle systems (Forward, Interior, and Aperture Hood) provide stray light control. The CIE controls the two APS detectors and is described in Sect. 3.3.1. The Door Latch release is the only WISPR mechanism. Most of the subassemblies are briefly described in Sect. 3

an anti-ram location but it is essential for providing the proper observations of the large-scale structures that are being measured by the other SPP instruments, including the sources for any energetic particle events. Efforts are under way to understand and minimize the risk to the instrument from the inner corona environment as we discuss in Sect. 2.4. The adoption of a two-telescope design is driven by the need to accommodate the FIELDS antennas (Bale et al. 2014, this issue), which are located in front of WISPR, just behind the heat shield. With a single wide-angle lens system, two of the antennas would intrude into the unobstructed FOV of the lens leading to unacceptable stray light levels. Covering the WISPR FOV with two lens systems allows a more efficient masking of the reflections from these antennas and enables the safe operation of the instrument. This is discussed in more detail in the optical design section (Sect. 3.1).

2.2 System Description

The WISPR instrument comprises two modules: (1) the WISPR instrument module (WIM), shown in Fig. 9, includes the structure, baffles, door, telescopes, focal plane arrays (FPA) and the camera interface electronics (CIE), and (2) the Instrument Data Processing Unit (IDPU) which consists of the Data Processing Unit (DPU) and the Low Voltage Power Supply (LVPS). The electronics functional block diagram is shown in Fig. 10. The WISPR Camera Interface Electronics (CIE) is an adaptation of the SoloHI electronics. The data is transferred from the WIM to the IDPU via a serial data interface similar to Camera Link, is compressed and packetized and is then transferred to the onboard Solid State Recorder via SpaceWire.

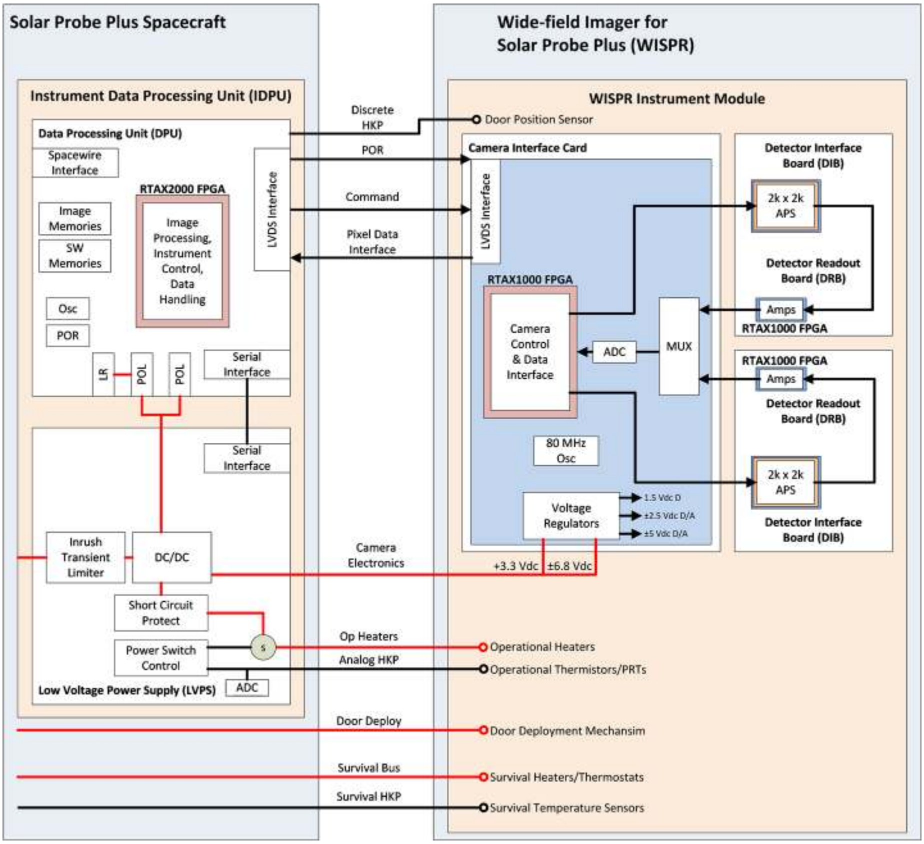

Fig. 10 WISPR Electronics functional block diagram. The IDPU (*left*) is located inside the spacecraft and is described in detail in Sect. 3.4. The CIE (*right*) is located on the WISPR telescope and is described in Sect. 3.3.1

The IDPU controls the two cameras, the door deployment and the operational heaters, receives the analog data, digitizes it to 14 bits, removes cosmic rays, and adds individual images together to increase SNR. The IDPU is described in detail in Sects. 3.4–3.4.2.

The WISPR instrument concept is in effect a miniaturization of the SECCHI/HI concept with adaptations from the SoloHI design. The WISPR telescope volume (54.3 (L) × 21.7 (W) × 26 (H) cm) is about 2.5 times smaller than the SECCHI/HI volume (72 (L) × 42 (W) × 24 (H) cm). It is the smallest Heliospheric Imager to date with capabilities that meet or even exceed the performance of the SECCHI/HI. It is a two-telescope system, similar to SECCHI/HI, with an inner telescope extending from 13.5° to 53° and an outer telescope extending from 50° to 108° (Fig. 9). The instrument uses the spacecraft heat shield as the first occulter and hence the alignment between the heat shield and the first occulter baffle, F1 is a critical element for the successful control of the stray light (see Sect. 3.1). The inner FOV cutoff is set at an elongation of 13.5° from Sun center, corresponding to a heliocentric distance of 2.3 R_s at 9.86 R_s perihelion. The cutoff is dictated by two requirements: (1) to remain within the heat shield umbra (8°, including a 2° maximum spacecraft offpoint), and (2) to accommodate the instrument on the spacecraft bus at a reasonable height and with reasonable mass. The overall instrument characteristics are shown in Table 3.

Table 3 WISPR instrument characteristics

Telescope Type	Wide-angle lenses, aperture stop placed in front of lens: Inner: $f = 28$ mm, aperture = 42 mm^2, 490–740 nm (bandpass) Outer: $f = 19.8$ mm, aperture = 51 mm^2, 475–725 nm (bandpass)
Plate Scale	1.2–1.7 arcmin/pixel (inner-outer)
FOV	95° radial × 58° transverse, inner field limit 13.5° from Sun center
Image Quality	Predicted RMS spot including allowable tolerances at 20° from boresight: Inner: 19.5 microns (2.34 arcmin) Outer: 19.9 microns (3.38 arcmin)
Detector	APS, 10 micron pitch, 2048 × 1920 pixels
Baffle Design/Stray Light Rejection	Front heat shield edge, forward baffle and diffraction light trap designed to reject incoming solar radiation, interior baffles and aperture enclosures designed to reject scattered solar radiation from spacecraft structures, and thermal radiation from antennas. Average predicted stray light: $<2 \times 10^{-9}$ B/Bs @ 9.86 R_S and $<2 \times 10^{-12}$ B/Bsun @ 0.25 AU, well below the K + F corona
Pointing	Instrument axes aligned to spacecraft to <0.5 deg, F1 and heat shield leading edge placement error <13 mm. Baffles achieve adequate rejection with 2° excursion from sun center at perihelion
Calibration	<20 % absolute radiometric, platescale <4 %, pointing: accuracy 5 arcmin (3σ), jitter 0.8 arcmin (1σ), windowed stability 1.6 arcmin (1σ)
Mass	WISPR Instrument Module (WIM) 9.8 kg; Instrument DPU (spacecraft provided) 1.1 kg
Average Power	7 W (including 4 W operational heater power)
Envelope	WIM Module: 58 cm × 30 cm × 46 cm (door closed)
Avg TLM Rate	Allocated data rate 26.6 kbps (during 10-day operational periods); 23 Gbits per orbit

A set of forward occulters (Forward Baffle Assembly) is located on a ledge to reduce the diffraction from the heat shield. An internal baffle assembly reduces this stray light component further as well as stray light diffracted from the FIELDS radio antennas and other spacecraft structures. Another set of baffles is located at the apertures of the two telescopes to prevent any further reflections from reaching the detectors. Because of the orbit profile, the WISPR stray light rejection requirements vary as a function of elongation angle and heliocentric distance by about an order of magnitude. The most stringent requirement is 1.8×10^{-12} B/B$_{\text{sun}}$ at the outer edge of the FOV (90° elongation) at the largest distance from the Sun (0.25 AU). The sophisticated baffle design allows WISPR to meet this requirement and allows for high signal-to-noise ratio (SNR) imaging ranging from SNR = 20 at the inner FOV at closest perihelion to SNR = 5 at the largest distance and FOV angles. The detectors are 2048 × 1920 format APS CMOS devices developed for the SoloHI program (Howard et al. 2013). APS devices are much less susceptible to radiation damage than the more common CCD devices and are therefore the best option for this mission. They also come with significant savings in terms of power and mass. These devices are described in more detail in Korendyke et al. (2013). The devices are cooled to −60 °C via a passive radiator. A one-shot door protects the baffles and optics from contamination during ground operations, launch, and early flight operations.

2.3 Assembly, Integration and Test

The instrument is calibrated at the component and subassembly level as well as "end-to-end" at the instrument unit level. Optical tests will ensure that the baffle surfaces and optical components meet requirements for efficiency, imaging and scattered light. The APS detector is calibrated for quantum efficiency, dynamic range, resolution, and noise. The instrument performance is tested/characterized in the dedicated NRL coronagraph test facilities that contain an 11 m beamline optical test chamber and Class 100 cleanroom. Additional baffling is added to the chamber to allow end-to-end stray light testing of stray light to $\sim 10^{-15}$ B/B$_{\mathrm{sun}}$, similar to the successful SECCHI/HI end-to-end stray light test. This test was the first test to successfully achieve this level of sensitivity. The chamber is equipped with collimating optics, a precision instrument pointing table and necessary light sources. The laboratory is equipped with optical benches, theodolites, alignment telescopes, optical flats, and light sources. Component transmission and reflectivity are characterized using a Cary spectrophotometer and spectroradiometer. End-to-end calibrations performed under vacuum include: vignetting, radiometric calibration (responsivity), image quality, wavelength range, stray light and flat field. End-to-end calibration activities use the instrument electronics in the flight configuration. All calibrations are directly traceable to NIST using secondary standards. The laboratory calibration and image quality measurements are validated on-orbit using a set of standard stars similar to the procedures we use on the SOHO/LASCO and STEREO/SECCHI instruments. The final calibration using the standard stars will be accurate to ~3 %, exceeding the 20 % absolute calibration requirement (Thernisien et al. 2006).

2.4 Environmental Challenges

We have little, if any, information for the environment SPP is going to operate in. It is reasonable to expect that the spacecraft will encounter high particle intensities, including elevated numbers of neutrons. The mission total ionizing dose (TID) of radiation is estimated to be 24 krad behind 100 mils (2.54 mm) of Al shielding.

The other concern is interplanetary dust. This is a novel concern for a heliophysics mission because SPP is the first spacecraft to receive dust impacts at a high orbital velocity, about 170 km/s at perihelion at a location where significant amounts of interplanetary dust are thought to be present. Unfortunately, we know little about the dust environment close to the Sun (see discussion in Sect. 1.4). The Helios measurements from 0.7 to 0.3 AU are the only available measurements (Leinert et al. 1981).

2.4.1 Radiation Effects

We used SPP radiation guidelines for a seven-year mission for EEE parts selection. Our designs address single event effect (SEE) induced failure (latchup, burnout, gate rupture, secondary break-down), non-destructive SEE (e.g., non-destructive latchup, minilatchup, and single event functional interrupts) and single eventinduced soft errors (including single event upsets (SEU) or transients in linear devices) and SEE-induced soft errors. All EEE parts meet the TID requirement with a minimum radiation design margin of 2× the mission TID (60 krad behind 100 mils of Al shielding). We use no EEE parts having a linear energy transfer (LET) threshold of <25 MeV cm^2/mg (SEU) or 100 MeV cm^2/mg. The selected APS detector technology (see Sect. 3.3.1) mitigates potential problems of Non-Ionizing Energy Loss (NIEL) and radiation-induced Charge Transfer Efficiency (CTE) losses. Unlike CCDs (LASCO, SECCHI/HI), the photoelectrons are read-out from each APS pixel without

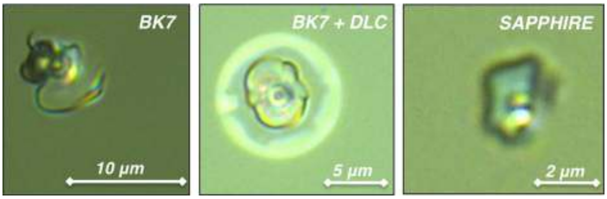

Fig. 11 Crater damage caused by dust impacts in the three glass types used in our testing. BK7 (*left*) is a commonly used glass type in space telescopes. BK7 with a diamond coating (DLC, *middle*) exhibits an additional ring around the crater possibly caused by coating separation from the glass. Sapphire (*right*) exhibited the least damage but it is an experimental glass type of unproven optical performance

shifting through the rest of the detector. Like CCDs, the radiation-induced damage increases the dark current, dark current non-uniformity noise in addition to particle-induced ionization transients ("cosmic rays" are scrubbed on-board as done on SECCHI/HI), temporal variations in pixel dark current and other effects.

2.4.2 Effects of High Speed Dust Impacts

Given the potentially high dust velocities, the kinetic energy distribution and fluence of the dust particles must inform the instrument design. Since the mass and size distribution is unknown close to the Sun, the design relies on the JHUAPL/UTEP models developed specifically for SPP (Mehoke et al. 2012). The model predicts about 100 impacts from 10-micron particles and 1000 impacts from 0.1-micron particles at the heat shield during the seven years of the mission. It also predicts that most particles will have diameters below 10 microns. Dust impacts can cause increased stray light levels for WISPR in two ways: (1) by damaging the edges of the forward baffles and, (2) by pitting or cratering the surface of the first lens. Additionally, there is an exceedingly small probability ($<10^{-5}$ for >1 mm particle) of a catastrophic hit by a large particle.

To understand the effects of dust on instrument performance, the WISPR team has undertaken a glass testing and modeling program during the design phase with the help of the German Co-Is (V. Bothmer, PI). The Dust Accelerator at the Max-Planck-Institut für Kernphysik (MPIK) in Heidelberg was used in October 2012 to test three different candidate glass materials for the WISPR optics: BK7, BK7 with a diamond-like coating (DLC), and sapphire. The tests were performed with a variety of iron particle distributions (0.5–3 microns) and speeds (0.5–8 km/s) against three different impact angles (0°, 45°, 70°).

The examination of the impacted glasses showed that sapphire was the most impact-resistant material with very small (2 micron diameter; Fig. 11, right) and relatively symmetric craters. The impacts resulted in an unexpected behavior for the diamond-coated BK7. They caused a halo around the impact crater (Fig. 11, middle) that was likely the result of the local detachment of the coating due to the heat produced by the impact. The regular BK7 has relatively small craters (∼5 micron diameter; Fig. 11, left). Overall, the spall diameters are very consistent with the APL/UTEP model and provide confidence in the overall SPP project dust analysis and risk mitigation procedures.

To access the extent of the damaged area we developed an automated software program to measure the size and numbers of craters in the images. The results (Fig. 12) show that sapphire is the most robust glass type. However, this type of glass has never been used for space applications before and therefore requires significant development. On the other hand, the standard BK7 suffered only modest damage and it is a well-known material for space options.

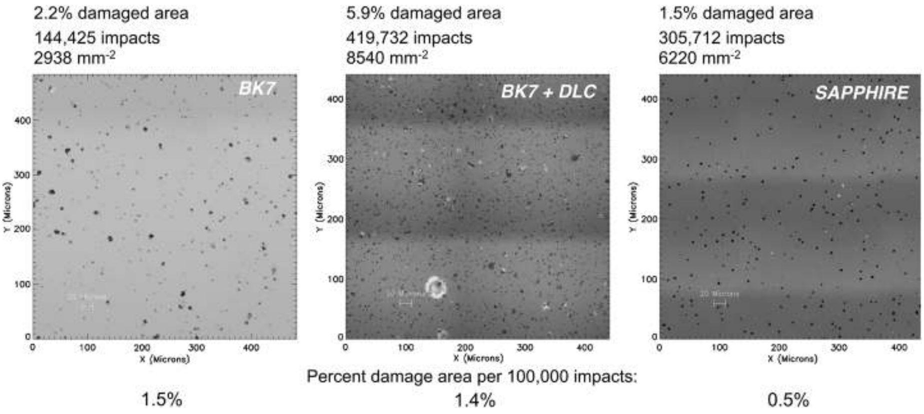

Fig. 12 Estimation of damage due to dust impacts for the three glass types. The statistics on the top of the figure are derived from the automated image processing software developed specifically for the dust testing. The normalized statistics (per 10^5 particle hits) are given in the *bottom*. The sapphire coating is clearly the most robust but it also has the least heritage and development

Since the dust testing was in agreement with the APL/UTEP dust model, we use the model to estimate the percentage of damaged area expected for the objective lens of the WISPR outer telescope, which has the most exposure to dust. The model predicts that 0.6 % of the lens area will be pitted by the end of the mission. This value, representing the worst-case scenario, is then adopted for both the inner and outer telescope objective lenses. To evaluate the effect on the imaging performance we first measure the change in the Bidirectional Scattering Distribution Function (BSDF) (or Harvey-Shack function) in the damaged glass relative to the pristine BK7 BSDF. The laboratory-measured BSDFs revealed that we made conservative assumptions in our stray light estimates during the design phase. Therefore, the stray light calculations for pristine and damaged WISPR lenses were rerun using the measured BSDFs. The resulting beginning and end of life optics performances are shown in Fig. 13.

To summarize, the dust testing has been very valuable for the WISPR design process. It validated the APL/UTEP model (for velocities ∼2–3 km/s), allowed to safely reject exotic materials and coatings as an alternative to regular BK7, led to the development of a realistic BSDF model for evaluating the stray light effects of dust impacts on the imaging performance, and provided an estimate on the approximate damaged area of the WISPR optics. Based on these results, the regular BK7 was adopted as the baseline for the WISPR optics.

3 WISPR Instrument Design

3.1 Optical Design

The instrument's telescope design is monolithic (with no moving parts) and uses radiation-tolerant glass lenses mounted in lens barrels. It is based on the SECCHI/HI design and consists of two telescopes, the inner and outer telescopes with the optical parameters shown in Table 4. The optical layout is shown in Fig. 14. The resolution is optimized for the FOV center, 33.5° and 79°, for the inner and outer telescope, respectively. BK7 was selected for the first lens element because it was shown to be sufficiently resistant to dust impacts (see

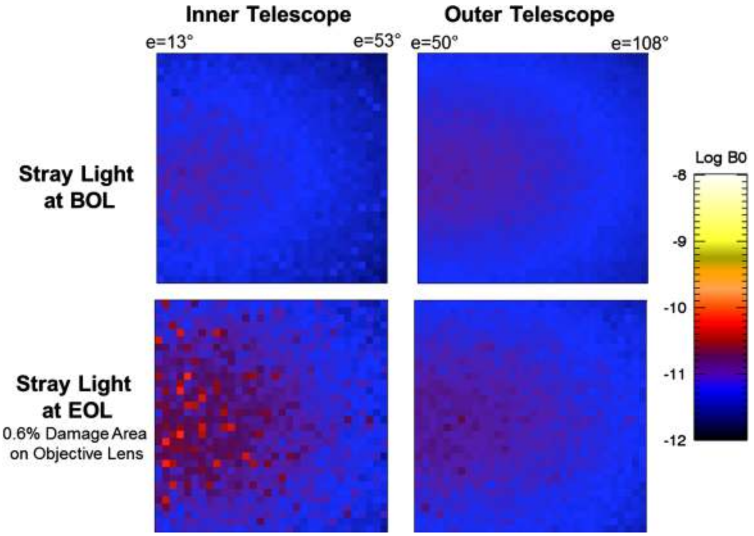

Fig. 13 *Left*: Model predictions of the stray light levels at Beginning-(BOL) and End-Of-Life (EOL) for the WISPR telescopes. The EOL predictions assume damage to 0.6 % of the lens area and use lab BSDF measurements from the dust-impacted glass. The higher levels in the inner telescope are a result of the much brighter scene at those elongations

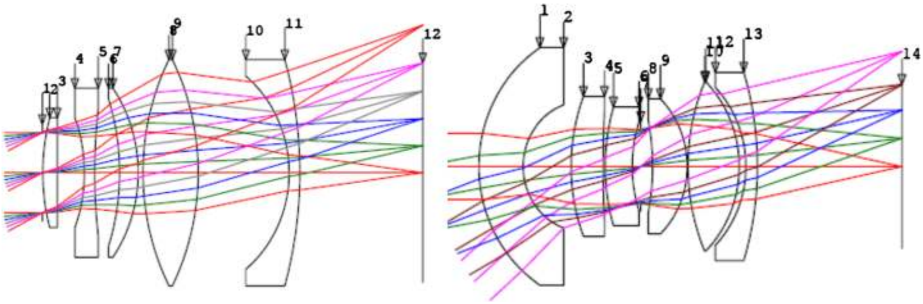

Fig. 14 WISPR lens assemblies for the Inner (*left*) and Outer (*right*) telescopes showing the ray tracing results through the various lens surfaces

Table 4 WISPR Optical Design

	FOV	Spectral Range (nm)	Entrance Pupil (mm)	F#	# of lenses	RMS Spot Size (μm)
Inner Telescope	40° × 40°	490–740	7.31	3.83	5-element	19
Outer Telescope	58° × 58°	475–725	8.08	4.04	6-element	20

Sect. 2.4). The bandpass for each telescope is selected using a combination of long/short wavelength cutoff filters deposited on internal lens surfaces similar to SECCHI/HI.

As can be seen from Table 4, the current optical design is excellent. It provides both fast lenses (low F#) and high spatial resolution (∼2 pixels) for the inner and outer telescopes,

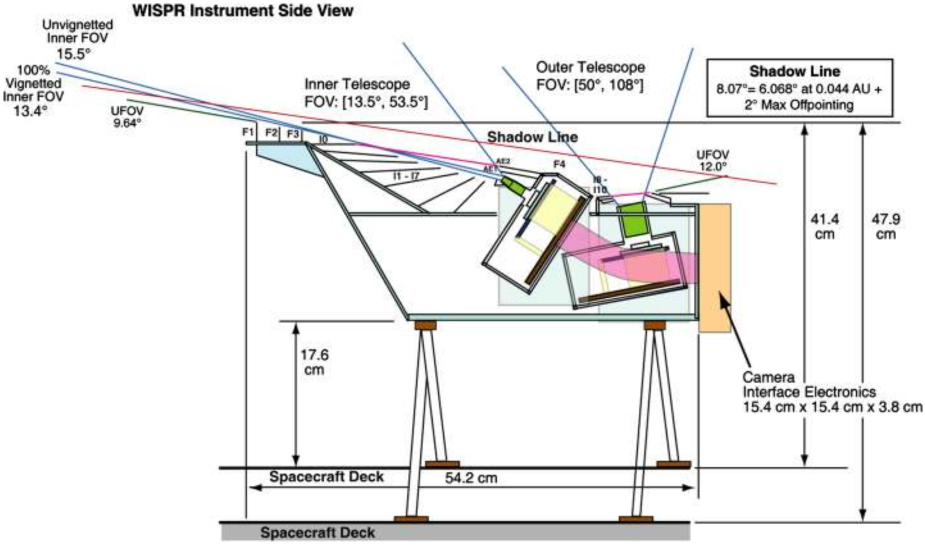

Fig. 15 Side view of the WISPR instrument showing the exterior (F1–F3) and interior (I1–I7) baffles, and the two telescope assemblies. The dimensions and FOV of the two telescopes and CIE are also shown. For instrument safety, no part of WISPR can exceed the shadow line even under the maximum possible spacecraft offpoint of 2 deg

respectively. This means that WISPR is potentially capable of capturing images at spatial resolutions of <2 arcmin (2200 km or ∼3 arcsec from 1 AU), which are comparable to eclipse imaging from Earth. This is truly remarkable for a wide-field coronal telescope and the capability will be exploited as mission and solar condition allow. However, the current observing plan is to obtain images with 2 × 2 binning, as is done for SECCHI/HI, to increase the SNR and reduce the telemetry load. Higher image binning (4 × 4) will be required at large heliocentric distances to maintain a minimum SNR of 5 at the outer edge of the FOV.

The baffle design (Fig. 15) rejects the incident solar radiation using a combination of the heat shield leading edge, front baffle assembly, and aperture light traps. Scattered radiation from the spacecraft is eliminated using the interior and peripheral baffle assemblies. The WISPR baffle design is based on the successful SECCHI/HI instrument design (Socker et al. 2000). The combination of the heat shield leading edge and the series of three linear occulters in the front baffle assembly attenuate the stray light that reaches the entrance aperture. Figure 16 shows the inner telescope normalized irradiance of the diffracted light from the heat shield/front baffle assembly combination at the worst off-pointing case of 2° during science operations at the minimum perihelion of 9.86 R_s. The worst-case diffracted stray light on the detector is predicted to be 7.5e-13 B/B_{sun}, which increases to 1.4e-11 B/B_{sun} when all the other sources of stray light are accounted for (dust damage on the first lens, F-corona, and scattering from the two FIELDS antennas). This is still 55 times lower than the requirement of 7.9e-10 B/B_{sun}. To deal with the sharp brightness gradient of the corona close to the limb, the last baffle (F3) in the forward baffle assembly imposes some vignetting of the innermost part of the Inner Telescope FOV from 60 % at 13.5° to 30 % at 14°. Also, the wide-field lens creates natural vignetting (increasing as $\cos^4$ of the angle from the boresight).

The aperture light trap, including baffles AE1 and AE2, closes out the aft side of the entrance aperture and defines the aft Unobstructed Field Of View (UFOV) angle. The aperture

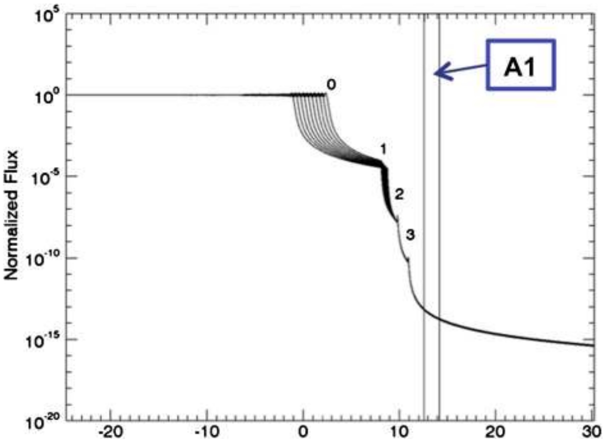

Fig. 16 Diffraction profile for the combination of heat shield and forward baffle system. A1 is the entrance aperture of the inner telescope

light trap captures diffracted light from the F1 and F2 baffles, but does not directly intercept any diffracted light from the heat shield leading edge. The aperture light trap baffles are oriented toward the forward baffles such that no single reflection from the light trap directly enters the A1 aperture. The peripheral baffles limit stray light from surrounding spacecraft surfaces entering the interior baffle cavity. Following STEREO/HI, the interior baffles are CFRP panels coated with Aeroglaze Z307 to attenuate reflected stray light in the instrument. In addition, the interior baffles are oriented to prevent any single reflection of scattered light from spacecraft surfaces outside the aft UFOV from reaching the A1 aperture.

The instrument is designed to remain below the direct solar radiation that comes over the heat shield leading edge from the sun disk edge throughout the entire SPP orbit for the worst-case off pointing. The shadow line in Fig. 15 defines this 8.07° solar exclusion zone based on the solar disk radius of 6.07° at the minimum perihelion of 9.5 R_S, the maximum failure mode off pointing of 2.0°.

The baffle design directly drives the instrument volume. The design uses realistic baffle tolerances (e.g. 80 µm Z/220 µm X for F2/F3 baffles to F1 baffle; heat shield leading edge to F1 baffle tolerance given in Table 3 WISPR Instrument Characteristics) based on SECCHI/HI and SoloHI experience. In addition, the instrument design includes a forward UFOV angle from the F1 baffle of 9.12° to avoid the heat shield leading edge for the worst-case tolerances. Overall, the current optical design meets the stray light requirements, even in the worst-case configurations of the FIELDS antennas and dust impacts.

3.1.1 Instrument Stray Light Control

The control of stray light due to spacecraft accommodations has been the major focus of the WISPR team during the preliminary design phase of the project. The WISPR imager concept was a single wide-field lens, requiring an UFOV of 180°. However, the FIELDS instrument needed to place its antennas on the sunward side of the spacecraft to sample the solar wind undistorted by the spacecraft charging effects. As a result, two of the antennas impinged either directly into the WISPR FOV or extended into the UFOV allowing diffracted sunlight to enter the aperture at unacceptable levels. In addition, the tips of the antennas will get so hot (∼1800 °C) that they will radiate in the visible region of the spectrum creating another (and novel) source of stray light. The only solution for allowing the instrument to operate was to baffle directly these two sources of stray light. In order to achieve this without sacrificing

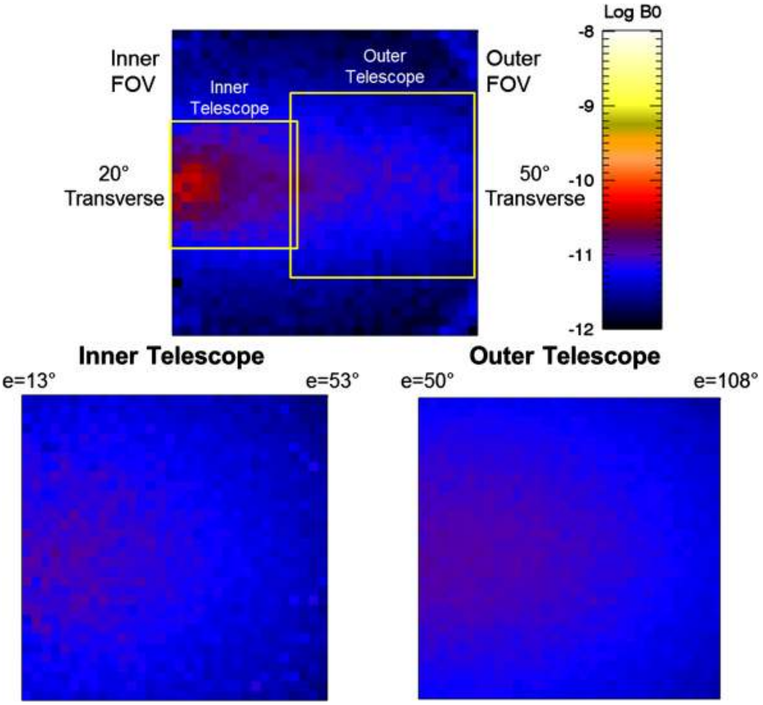

Fig. 17 *Left*: The improvement in stray light levels resulting from the single (*top panel*) to two-telescope (*bottom panels*) design change and from the optimization of the peripheral baffles

most of its FOV, the WISPR field-of-view was split into two separate imaging assemblies as discussed above.

This change allowed the design of peripheral baffles that capture the diffracted and radiated light from the antennas and reduce the stray light to acceptable levels as shown in Fig. 17. This is a preliminary result, however. The stray light modeling is performed via Monte-Carlo techniques with the FRED Optical Engineering software using a CAD model of the instrument and FIELDS antennas. This approach allows not only the modeling of the antenna diffracted and radiated light but also the testing of various coatings for the baffle surface and even the modeling of the effects of dust impacts during the mission as we see in Sect. 2.4. These new stray light modeling methods, driven by the need to accommodate occulting-like imagers in crowded spacecraft environments, far exceed the corresponding modeling efforts in past coronagraphs and imagers where tight controls of structure intrusions in the UFOVs were possible. They demonstrate that visible light imagers can be accommodated and operate safely even when structures intrude into their direct UFOVs.

3.2 Mechanical Design

The WIM consists of a primary structure made from composite facesheets with a honeycomb core, which encloses two Focal Plane Assembly (FPAs) boxes, holding the detectors and detector readout boards (DRBs), two boxes for the baffles (interior and forward) and a plate for the peripheral baffle. In addition, the CIE is contained in a box attached to the rear of the primary structure and the radiators are mounted to the right side. The door mounts to the top and opens to the left (Fig. 9).

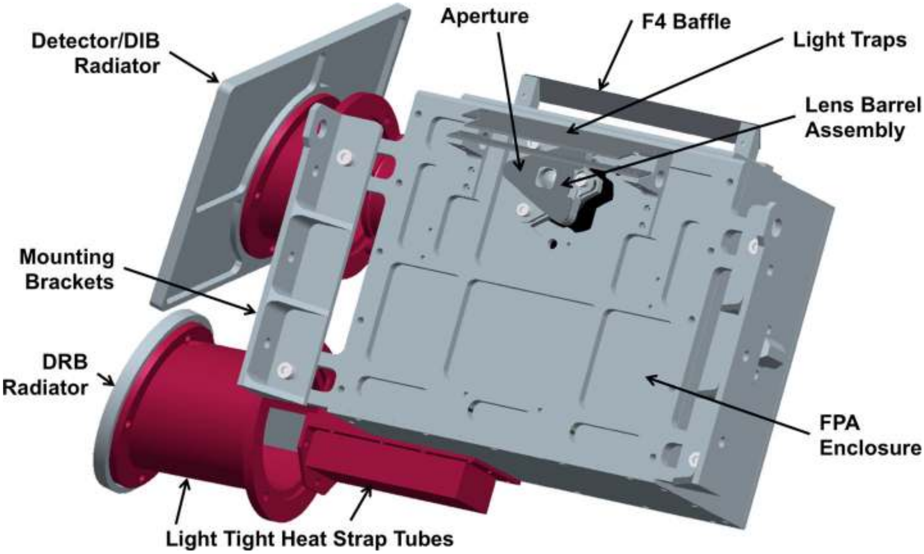

Fig. 18 The mechanical design of the Inner Telescope FPA showing the main components of the FPA. The F4 baffle provides additional stray light rejection for the Outer Telescope

Focal Plane Assembly (FPA) The FPA provides physical mounting, optical positioning, electrical connections, and thermal cooling for the APS detector (Fig. 18). The WISPR FPA design is a slight modification to the SoloHI FPA to account for the smaller detector, the APS control electronics, a warmer operating temperature, and a shorter distance to the radiator plate. The APS detector is cooled passively by conducting heat through a cold finger to a radiator with a view to deep space. A 10 °C temperature drop between the radiator and the detector is expected based on the SECCHI/COR2 performance. No difficulties are expected on obtaining temperature <-55 °C since the SECCHI/COR2 CCD is operating at <-70 °C.

Baffles The mechanical design incorporates three baffle systems (forward, interior, and peripheral), all of them made of Al 6061. The forward baffles are attached to the truss structure with a series of clips and include shims for individual baffle alignment. The clips and screws are located on the outside edge of the baffles well outside the FOV. The interior baffles are assembled as a unit, which is then is mounted in the interior of the primary structure via pivot mounts on the sides and a mounting flexure in the front with shimming capability. The function of the peripheral baffle (or aperture hood assembly in Fig. 9) is to prevent stray light from the FIELDS antennas entering into the instrument. It is basically an Al plate with cutouts around the two telescope apertures. Those cutouts define the FOV of the instrument.

Door The one-shot WISPR door is a slight modification of the SoloHI door (Fig. 19). It is composed of several CFRP layers. The door blank is made using an invar mold for coefficient of thermal expansion (CTE) matching. It is mounted on the primary structures via two hinges. The Ejection Release Mechanism (ERM) is the sole WISPR mechanism (Fig. 19, right). It is a shape memory release device with a redundant firing circuit.

Instrument Mounts WISPR is mounted on the $+X$, $+Y$ (ram-side) panel of the SPP spacecraft with four bipod mounts (Fig. 20). The SPP spacecraft is a hexagonal design and hence

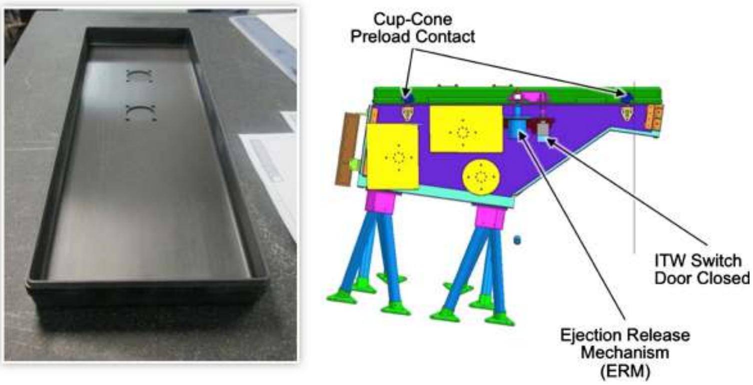

Fig. 19 *Left*: The SoloHI door. *Right*: Mechanical components of the door shown on the SoloHI instrument. The WISPR and SoloHI doors will be identical except for size

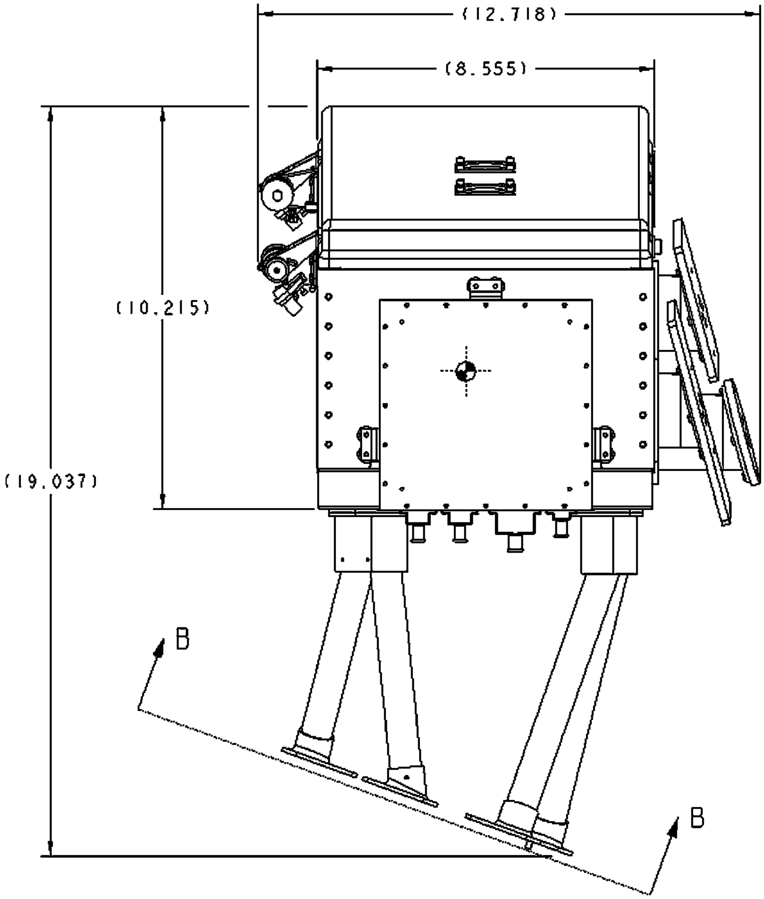

Fig. 20 View of WISPR from the rear of the spacecraft showing its orientation relative to the $+X+Y$ panel

there is no panel facing directly towards the ram direction. WISPR is rotated by −20° about the Z relative to the panel to optimize the coverage of structures to be encountered by the spacecraft. The somewhat unconventional adoption of two legs per mount (hence bipod) provides the necessary stability. The composite (Ti-Al) tube mounts keep the instrument primary structural frequency >80 Hz, address CTE mismatch between panel and instrument, and maintain the instrument to spacecraft alignment.

3.3 Electrical Design

The WISPR electrical design builds upon the SoloHI development program and consists of two major components: the Camera Electronics (CE), provided by NRL, and the Instrument Data Processing Unit (IDPU), provided by the Johns Hopkins University/Applied Physics Laboratory (JHU/APL). Each component comprises several subsystems, which we describe briefly below.

3.3.1 Camera Electronics

The WISPR Camera Electronics control and read out the APS detectors for both telescopes and send raw camera images to the IDPU for processing. They consist of the Camera Interface Card (CIC), which communicates between the IDPU and the two telescopes, and the image acquisition circuitry for the two telescopes. The latter comprises the APS detector, the Detector Interface Board (DIB) and the Detector Readout Board (DRB) enclosed within the FPA for each telescope (Fig. 10).

Camera Interface Card The CIC provides the electrical interface to the IDPU, routing of command/telemetry within the instrument, coordination of the inner/outer telescope readouts, signal chain and 14-bit A/D conversion of video from the two telescopes, and local analog telemetry acquisition. An RTAX1000SL FPGA provides the logic for the CIC. The CIC supports a Camera Link Interface (CLI) to GSE for early testing, and an interface to the IDPU, which provides: (1) a Command/Telemetry serial interface with 3.3 V LVDS async UART 19.2k BAUD, and (2) a serial pixel interface (SPI) with LVDS interfaces for serial header and video, 40 MHz clock, and DVAL/LVAL/FVAL signals sent to the IDPU. The SPI supports a 2 Mpixels/sec readout with a ≤ 256 bytes header.

Active Pixel Sensor The WISPR imaging detector is based on the Active Pixel Sensor (APS) developed by Sarnoff Corporation for the SoloHI investigation (Fig. 21).

Table 5 summarizes the WISPR APS imaging specification. The detector is radiation-hardened (operational after >1 Mrad exposure), has excellent performance in read noise, dark current, and full well capacity, and simplifies the drive electronics compared to CCDs. The APS detector includes the readout preamplifiers, the Double Correlated Sample and Hold circuitry, multiplexers and switches to access and read individual pixels. The capability to access individual pixels nearly eliminates the charge transfer efficiency (CTE) degradation from radiation damage and the image smearing in shutterless operation, present in the SECCHI/HI images. The device can operate under two gain modes: a high gain mode with full well $>120{,}000\ e^-$ and $\sim 40\ e^-$ read noise, and a low gain mode with full well $>20{,}000\ e^-$ and $\sim 7\ e^-$ read noise.

The WISPR APS detector utilizes the detector designs developed by the Solar Orbiter SoloHI program. The pixel design had been advanced in a series of ‘sandbox’ test runs under a Sarnoff development program (Korendyke et al. 2013). The performance of the detectors before and after radiation has been evaluated and documented during the SoloHI

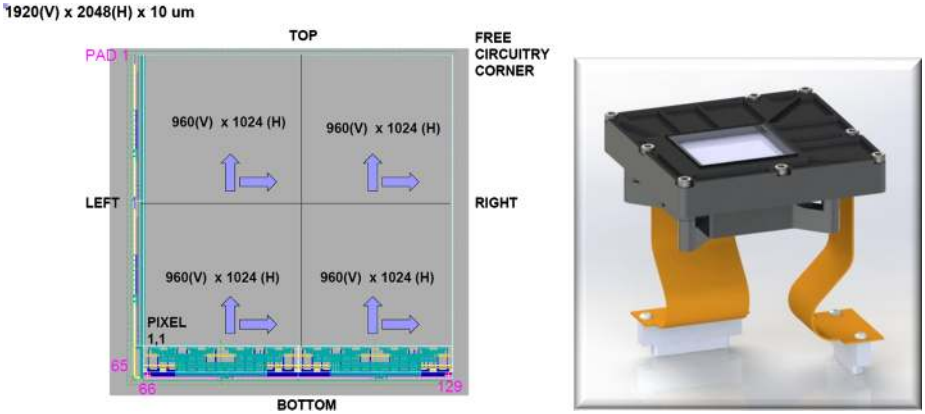

Fig. 21 *Left*: WISPR APS Detector Design. The *top* and *bottom* halves (960 × 2048) can be read independently. *Right*: The APS/DIB flight package. The *two yellow flex cables* connect the sensor to the DRB

Table 5 WISPR APS Detector Performance Capability

Parameter	Capability
Format	2048 × 1920
Pixel (size, type)	10 µm, 5T PPD
Operating Temperature Range	<-55 °C
Technology	Jazz 0.18 µm
Power	<500 mW at 3.3 V
QE	>34.3 % average over 470–755 nm
Radiation Tolerance	Tested to 100 Krad
Read Noise (EOL, 95 % of pixels)	7–13 e^-/pix
Dark Current (EOL, 95 % of pixels)	1.57–1.9 e^-/s/pix
Linear Full Well (95 % of pixels)	20,000–21,300 e^-/pix
Readout Rate	2 Mpix/s
Digitization	14-bit ADC
Cosmetics	95 % of pixels meet EOL requirements
Readout Modes	Progressive scan, global reset
Redundancy	Independent operation of each 960 × 2048 half

development program. The result of these tests raised the maturity level to TRL 6. To minimize dark current and potential radiation damage, the detectors will operate at moderately low temperatures (<-55 °C) using a cold finger passive radiator. The flight device fabrication has been completed and the selection and burn-in of flight candidates is underway. The WISPR program requires at least 4 flight devices (2 flight models and 2 flight spares).

Detector Interface and Readout Boards (DIB/DRB) The DRB generates the readout sequencing and collects the raw video from the DIB, sets the (adjustable) bias signals for the APS, monitors the detector temperature and controls the operation of the calibration LEDs. An RTAX1000SL FPGA provides the logic for the DRB.

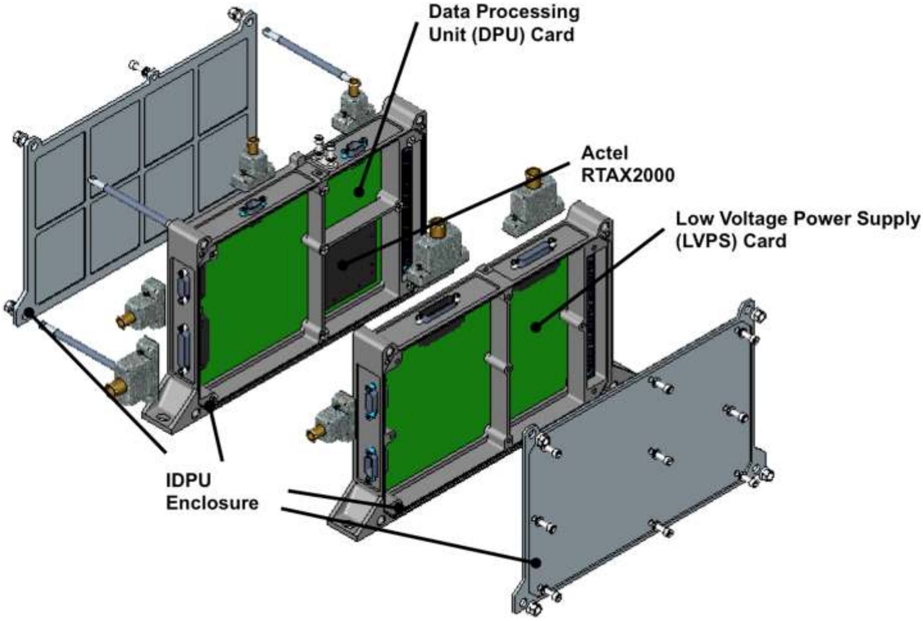

Fig. 22 The WIPSR Instrument Data Processing Unit comprises two cards (DPU and LVPS) in a Magnesium alloy enclosure

Each DIB is connected to the DRB via a rigid flex cable. The DRBs handle the readout of the image and all associated time-critical tasks, such as changing camera settings, clearing the detector, and handling the pseudo-rolling shutter.

3.4 IDPU Overview

The IDPU is mounted internal to the Solar Probe Plus, on the inside of the bulkhead to which the WIM is mounted (Fig. 8). It is a two-slice assembly consisting of the Data Processing Unit (DPU) slice and the Low Voltage Power Supply (LVPS) slice enclosed in a Magnesium Alloy package (Fig. 22). The LVPS provides secondary power to the WIM and the DPU. It receives 28 V switched power from the spacecraft and provides power control for the operational heaters. The DPU provides the primary interface to the spacecraft, breaking complex scheduled command sequences into primitive operational commands for the two cameras. The DPU commands the WIM, processes, compresses and, stores the WISPR images, distributes and collects housekeeping information and communicates with the spacecraft. The DPU also controls the operational heaters. The spacecraft controls survival heater power to the WISPR instrument directly and provides the door opening service. The WISPR IDPU derives its heritage from similar units on RBSP, CRISM and, MESSENGER.

3.4.1 IDPU Electrical

Figure 23 shows the connections from the spacecraft to the WIM, which consist of 9 cables. There is a power cable from the spacecraft to LVPS, 2 SpaceWire cables from the spacecraft to the DPU, a power cable from LVPS to WIM, Camera Interface cable from WIM to DPU,

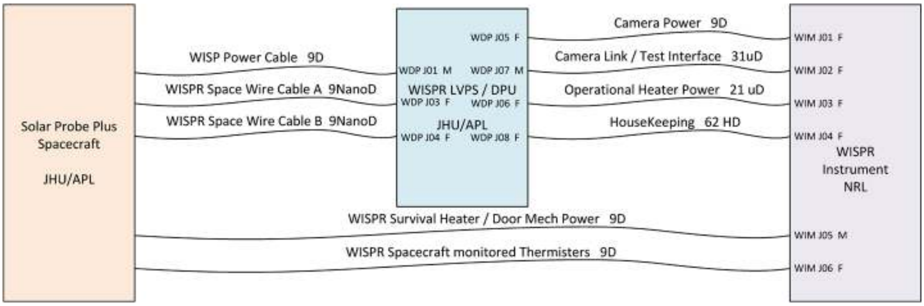

Fig. 23 Spacecraft-IDPU-WIM Harness and connectors. The functionality of each cable is also shown

operational heater cable from LVPS to WIM, housekeeping cable from WIM to IDPU, survival heater cable from spacecraft to WIM, and the spacecraft-monitored thermistors from WIM to spacecraft.

Figure 24 shows the electrical block diagram of the WISPR IDPU. The LVPS is implemented on a single 6.5″ × 4″ board and contains an inrush transient limiter, EMI Filter, a DV-to-DC converter (5VDC to IDPU, 3.3VDC digital and ±6.6 VDC analog supplies to WIM), heater switch control, housekeeping ADC System, and convertor synchronization and ADC system control (provided by the digital board).

The DPU is implemented on a 6.5″ × 4″ board and contains point-of-load convertors, memory modules for the processor and data processing and an Actel RTAX2000 FPGA. The DPU FPGA contains the SKIP processor, which is a programmable FORTH processor, the Image processor, and all the attached interfaces as shown in Fig. 24. The image processing is performed by hardware in the FPGA. The SKIP processor handles housekeeping, and manages the image processor based on schedules commanded by the ground. The FPGA contains:

- Clock and Reset distribution to generate Master Reset from redundant power-on reset chips, External Test Reset, and Internal Watchdog.
- 30 MHz SpaceWire and image processing clock.
- 7.5 MHz SCIP processor clock.
- Multiple memory interfaces.
- Image processor w/digital scope accessible test port.
- SCIP processor.
- Core I/O, which includes: Camera/Test UARTs, LVPS controls for heater switches and housekeeping ADCs, Voltage supply clocks, RMAP and SpaceWire node, and a40 MHz LVDS camera interface (FIFO to image processor).

All image processing takes place in the image processor (Fig. 25). The processor contains modules for common operations such as bias subtraction, pixel binning, compression, and packetization as well as modules specific to WISPR operations such as frame summing and a cosmic ray scrub operating on two images at a time. It has access to a 3 Gb SDRAM image storage, a 160 Mb SRAM image buffer, and 33.75 Gb of flash bulk storage, sufficient to store the full WISPR data volume for two orbits. The data are transferred to the spacecraft via SpaceWire at an average rate of 250 kbps.

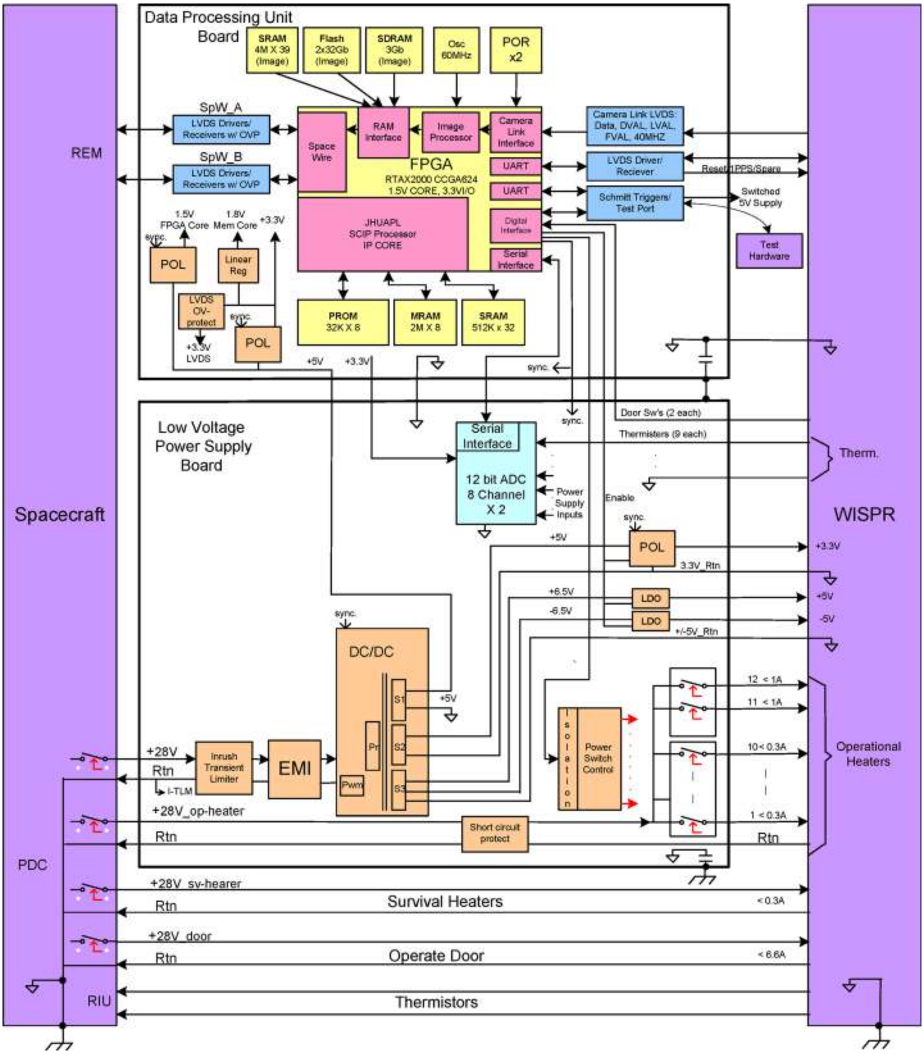

Fig. 24 A detailed WISPR IDPU Electrical Block Diagram. Section 3.4.1 provides only a top-level description of the IDPU functionality

3.4.2 IDPU Mechanical

The overall IDPU dimension is 21.2 cm (L) × 11.6 cm (H) × 5 cm (D). It weighs 1070 g and consumes 7.3 W (current best estimate). It is designed to operate between −25 °C and 65 °C and survive from −30 °C to 70 °C. The chassis, covers and shielding plate are made of 20 mm thick Mg ZK60A and is put together using Ti alloy (6AL4V). The preliminary structural analysis shows that the primary box and board modes are 192 Hz and 150 Hz, which exceed the 80 Hz minimum frequency requirement and demonstrate sufficient frequency separation.

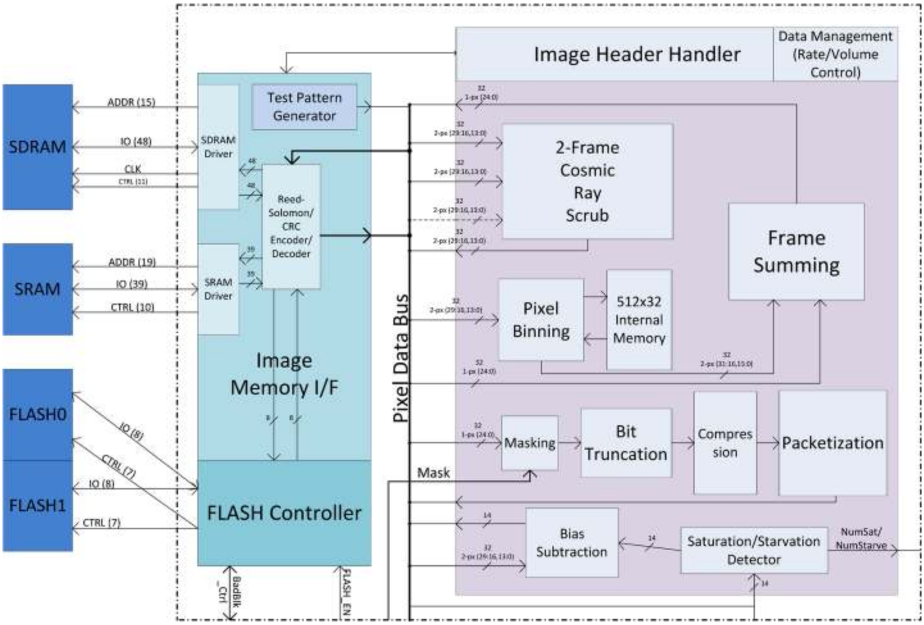

Fig. 25 Image processor Block Diagram showing the planned functions (cosmic ray scrubbing, image summing, binning, compression, packetization)

4 Science Operations, Data Processing, and Data Products

4.1 Description of Observations

4.1.1 Nominal Science

Routine observations to meet the science objectives occur during a window of ∼10 days duration centered on perihelion when the spacecraft is within 0.25 AU of the Sun (see Table 6). The standard image capture method takes short exposures (<20 seconds) and sums up to 'N' individual exposures to achieve the required integration time using on-board processing for image summing and "cosmic ray" scrubbing techniques that were developed and used on SECCHI/HI. The instrument is operated primarily in a synoptic observing mode, and similar observations are conducted each orbit using preplanned schedule blocks uploaded in advance of each encounter. Special observations tailored to specific science objectives are conducted on selected orbits (e.g. close to the minimum perihelion or with favorable geometries of Earth or other missions). Data are stored on the SPP solid state recorder (SSR) for transmission to the ground. A subset of the SSR data is transmitted at higher priority to facilitate planning for the next orbit.

Table 7 shows an observing program that is designed to fulfill the mission requirements for the final orbit in the nominal mission (Orbit 24). Many of the baseline science measurement requirements (including radial scene coverage, photometric accuracy, image cadence, and science observation days for the orbit and mission) depend on the instrument distance from the Sun. For this reason, the observing program over the solar encounter period is divided into the following four regions based on spacecraft distance from the Sun: *Perihelion*: <0.07 AU; *Inner*: 0.07–0.11 AU; *Mid*: 0.11–0.18 AU; *Outer*: 0.18–0.25 AU.

Table 6 WISPR Operational Timelines

Mission Event	Duration	WISPR Operations
Launch and Early Operations	Launch to first Venus encounter (L + 6 weeks)	Initial power on, IDPU, camera and FSW checkout, door-closed commissioning
Approach to First Solar Encounter	First Venus Encounter to First Solar Encounter (L + 6 weeks to L + 3 months)	Checkout/commissioning to prepare for science observations
Approach to Subsequent Solar Encounters	10 days per orbit for 23 orbits (spacecraft to Sun distance <0.5 AU) on inbound segment of orbit	Checkout, detector annealing, and on-orbit calibration to prepare for science observations
Solar Encounters	10 days per orbit for 24 orbits (spacecraft to Sun distance <0.25 AU)	Synoptic and tailored science observations
Aphelion Orbit Segment	68–130 days per orbit for 24 orbits (spacecraft to Sun distance >0.25 AU)	None (data downlinked when spacecraft to Sun distance >0.59 AU)

The highest cadence, full-FOV and partial-FOV observations are taken over a 36-hour period centered on perihelion. At larger distances from the Sun, the image cadence is reduced to satisfy the Level 1 photometric accuracy requirement. The observing program, including science data, housekeeping data, and CCSDS packet overhead, is constrained to fit within the WISPR data volume allocation of 23 Gbits for each orbit.

4.1.2 Early Operations and Commissioning

During launch and early operations (until the first Venus flyby, ∼6 weeks after launch), WISPR anticipates only door-closed operations, consisting of initial turn-on of camera subsystems, flight software (FSW) checkout and a few calibration lamp images (Table 6). The door remains closed during this time and throughout the SWEAP commissioning slew to permit outgassing of the instrument and spacecraft and to maintain survival temperature with minimal heater power. WISPR door-open commissioning operations are conducted in the interval between the first Venus flyby and the first solar encounter (∼6 weeks duration).

4.1.3 Calibration

We plan a limited set of observations for instrument checkout and calibration following instrument turn-on on the approach to each solar encounter. A few images per day will be taken for up to ten days while the spacecraft distance from the Sun is less than 0.5 AU on the inbound segment of each orbit. Some of these images may involve small off-points of the spacecraft from the Sun (up to a few arc minutes) to verify the stray light performance of the instrument. These data would need to be downlinked prior to the solar encounter period to be useful for planning purposes.

For photometric calibration, WISPR compares selected background stars in the images to star catalog positions and magnitudes. Thanks to the wide FOV of WISPR, no spacecraft maneuver is required to capture a standard set of calibration stars. These calibrations are used to verify the pre-launch ground photometric calibration and to monitor the WISPR telescope throughput loss during the mission. The final photometric calibration accuracy using standard stars is ∼3 %, based on procedures developed and used for SOHO/LASCO and

Table 7 WISPR Example Observing Program for SPP Orbit 24

			WISPR Telemetry Requirement				
Observing Region	**Image Type**	**Radial FOV**	**Image Cadence**	**Daily Image Count**	**Daily Data Volume (Gbits)**	**Orbital Data Volume (Gbits)**	**Avg Data Rate (kbps)**
Encounter 10 days						**23.0**	**26.6**
Perihelion 1.5 days	**Total**				**7.93**	**11.90**	**91.8**
	Full Frame	13.5° to 108°			**4.71**	**7.06**	54.5
		13.5° to 38.5°	2.5 min	576	2.25	3.37	
		38.5° to 53.5°	5.0 min	288	0.67	1.00	
		50° to 79°	5.0 min	288	0.95	1.42	
		79° to 108°	7.5 min	192	0.85	1.27	
	Inner FOV Subframe	13.75° to 20°	5.5 sec	3927	**2.80**	**4.20**	32.4
	Housekeeping		10 sec		**0.028**	**0.041**	0.32
	CCSDS				**0.39**	**0.59**	4.5
Inner 1.5 days	**Total**				**3.60**	**5.40**	**41.7**
	Full Frame	13.5° to 108°			**3.39**	**5.09**	39.3
		13.5° to 38.5°	5.0 min	288	1.60	2.39	
		38.5° to 53.5°	10.0 min	144	0.47	0.71	
		50° to 79°	10.0 min	144	0.79	1.18	
		79° to 108°	15.0 min	96	0.54	0.81	
	Housekeeping		10 sec		**0.028**	**0.041**	0.32
	CCSDS				**0.177**	**0.266**	2.1
Mid 3.0 days	**Total**				**1.08**	**3.25**	**12.5**
	Full Frame	13.5° to 108°			**1.00**	**3.00**	11.6
		13.5° to 38.5°	15 min	96	0.53	1.60	
		38.5° to 53.5°	30 min	48	0.16	0.47	
		50° to 71.75°	30 min	48	0.21	0.62	
		71.75° to 108°	30 min	48	0.11	0.32	
	Housekeeping		10 sec		**0.028**	**0.083**	0.32
	CCSDS				**0.053**	**0.160**	0.6
Outer 4.0 days	**Total**				**0.63**	**2.44**	**7.1**
	Full Frame	13.5° to 108°			**0.57**	**2.21**	6.4
		13.5° to 38.5°	20 min	72	0.40	1.60	
		38.5° to 53.5°	40 min	36	0.05	0.19	
		50° to 71.75°	40 min	36	0.05	0.19	
		71.75° to 108°	40 min	36	0.08	0.23	
	Housekeeping		10 sec		**0.028**	**0.111**	0.32
	CCSDS				**0.031**	**0.120**	0.35

STEREO/SECCHI. Between perihelion passes, a three-phase calibration sequence must be performed: (1) to determine if any degradation of the detector and/or the lenses occurred during the perihelion pass, where the instrument might be subjected to high radiation exposure, (2) to anneal the APS detector, and (3) to perform a calibration sequence to determine the pre-perihelion calibration. Photometry changes are fixed by the stellar transits combined with LED calibration lamp images.

4.2 Flight Software

The WISPR Flight Software (FSW) is developed by the APL IDPU team. It incorporates considerable heritage/commonality from other missions such as MESSENGER, MRO/CRISM, New Horizons, and Solar Orbiter/SIS. The common software makes use of heritage boot code, telemetry and command packet handling, macro (stored command script) implementation, memory management, autonomy, and reporting modules. The data interface with the spacecraft is SpaceWire and has a SPP-specific protocol with static bus schedule and Instrument Transfer Frames. Telemetry packets may be up to 4096 bytes and there are 64 APIDs available for WISPR to use for addressing destination. There is a critical status packet monitored by the spacecraft, which can request power off or power cycle. WISPR receives time and status from SPP at 1 Hz.

Software that is WISPR-specific includes camera control, image processing, observation scheduling including autonomous operations, and instrument health. There are 12 independently controlled operational heaters. The observation schedule time line is loaded prior to the start of the encounter. The concept is similar to the time line developed for the STEREO/SECCHI instrument. All the parameters of the time line are loaded—image time, exposure duration, number of images in the sum, subimage coordinates, image compression, etc. To smooth out the telemetry flow to the spacecraft a large memory buffer has been included on the instrument side of the interface. The size of the buffer is sufficient to store the data from more than one orbit. No ability to perform selective data transfers to the spacecraft data recorder is envisioned.

Camera operation involves loading, starting, and stopping various instances of "microcode", and setting various registers which determine certain observations parameters. There are also calibration LEDs which need control. Most of the image processing is done in hardware (FPGA) and is orchestrated by the FSW. The possible image processing steps are: bias subtraction, clipping (max/min), cosmic ray scrub, divide by $2\times$, autonomous exposure control, pixel binning, image data compression (lossy or lossless), apply mask, and sum multiple images.

Image files received from the FPGA, including headers, are put in packets and assigned ApIDs to specify destination and downlink priority. The FSW must also manage 3 areas of image memory: (1) 156 Mb SRAM serves as an image output buffer (2) $\sim$3 Gb of SDRAM is available for image processing and secondary image output buffer (3) 64 Gb of Flash memory is available as tertiary image output buffer, if required. The SpaceWire output to spacecraft is limited to 350 kbps. For observation scheduling, the FSW must conduct activities such as load microcode, specify to FPGA what processing is to be done with each image received from the camera, implementing post-FPGA processing, and handle image telemetry priorities. Since this is an encounter mission with limited contact, the scheduling must be tolerant of instrument power cycles. Hence, the nominal mode of operations is "Autonomous Mode" where observations are resumed at the current mission experiment time. It is possible to specify that WISPR boot into "Manual Mode" where commanding is required to conduct operations.

4.3 Mission Operations

The detailed observing schedule will be uploaded prior to the beginning of each perihelion pass. However, there may not be sufficient time to modify the detailed schedule for the upcoming perihelion passage after the download of the SRR from the preceding pass. For this reason, the observing objectives are defined for the next two perihelia.

The cruise/downlink portion of each orbit is broken into either cruise operations or science downlink operations. For cruise operations, the instruments may be powered on if the Sun-spacecraft distance is less than 0.82 AU. Periodically, during cruise operations the instruments may be powered off to support routine and special spacecraft activities. During

Table 8 SPP DSN Contact Frequency

Mission Phase	Contact Frequency	Duration
Launch & Initial C/O Spacecraft	Continuous	2 weeks
Early Commissioning	5 × 10 hr (per week)	4 weeks
Cruise Operations	3 × 8 hr (per week)	Weekly
Science Downlink	10 hr/day	Entire science downlink period (Varies in each orbit leg, ∼4–21 days)
Solar Encounter Phase	3 × 4 hr (per week)	Entire encounter period (∼2 weeks)
Venus Fly-Bys	5 × 10 hr (per week) 10 hr/day	V − 5 to V − 1 weeks V − 1 to V + 1 weeks

cruise operations the fanbeam antenna (via X-band) will be used for spacecraft communications. Downlink rates will be limited and there is no plan to playback the SSR data.

During science downlink operations all instruments will be powered off and the high-gain antenna (via Ka-Band) will be used for playing back the SSR and retrieving all of the science data collected in the previous encounter(s). During both the cruise and science downlink periods, real-time spacecraft commanding will be done as needed to support routine and special spacecraft activities.

Table 8 outlines the planned DSN contact frequency for all phases of the SPP mission.

Part of the planning process entails assigning downlink priority to telemetry. The SPP supports up to 10 levels of priority for downlink; a small percentage of science data comes down relatively quickly (days) after an observing window. The majority of science data comes down at lower priority and could take months to reach the ground. These priorities may vary from orbit to orbit and are managed by the SWG.

4.3.1 Science Operations Center

The WISPR Science Operations Center (SOC) at NRL utilizes the GSEOS software suite provided through APL to send command files to the SPP Mission Operations Center (MOC) for uplink to the spacecraft. At the SOC, WISPR personnel utilize a Heliospheric Imager Planning Tool (HIPT) to model observation plans and translate them to schedule files that are uploaded to the WISPR IDPU.

4.3.2 Data Processing

The SOC receives real-time telemetry from the MOC via socket connection, or playback telemetry in Level-0 files transferred by SFTP. Housekeeping telemetry is translated into database scripts that populate a MySQL relational database. Science telemetry is captured from Level-0 packet files into compressed-image-files, which are processed in the Image Processing Pipeline (IPP) to Level-1 FITS files. These files, along with browse data and other data products, will be made available publicly via the WISPR website. WISPR Data Analysis Tools (DAT) will also be made available online via the Solarsoft library.

4.4 Data Products

NASA categorizes Data Products based on a system of Levels starting with Level zero. A level zero data product is usually defined as representing raw, but cleaned spacecraft

Table 9 WISPR Data Products

Data Level	Product Title	Contents	Format	Latency	Frequency
L1	Level-1 quick-look	uncalibrated image data	FITS	T_0 + minutes	as received; track-dependent
L1	Level-1 final	uncalibrated image data	FITS	T_0 + 7 days	per orbit
L3	Browse images (quick-look and final)	uncalibrated binned images with background removed, and compressed	PNG, JPG	L1+ minutes	same as L1
L3	Browse movies	browse images	MPG	L1 + hours	same as L1
L3	Jmaps	time-elongation plots, uncalibrated	PNG	L1 + hours	same as L1
L3	Syncronic or Carrington maps	heliospheric brightness at selected elongation angles	PNG	L1 + hours	same as L1
L2	Level-2	calibrated L1, user-generated	FITS	User-depended	as needed
L4	CME masses		FITS	T_0 + one year	Annually

telemetry. Subsequent data levels represent successive levels of data processing involving calibration and the application of science algorithms. The SPP mission has defined five data levels that are described elsewhere.

After generation of the Level-1 FITS files, selected Level-3 products (mostly browse data) will also be generated in the IPP. Level-2 (calibrated) products will be generated on-the-fly by using routines in the *Solarsoft* library. The best-available calibration will be made available to users as it is obtained via *Solarsoft*. Most of the code in the IPP will be available in the Solarsoft library. This data product philosophy follows closely the SECCHI data model. Table 9 summarizes the various WISPR data products.

The WISPR L1 quick-look data comprises two parts. Part 1 will be a subset of the images (such as subfields) sent down with low-latency to assist in planning selective downlink for other instruments and for planning WISPR observations for the next orbit. Part 2 of the quick-look data will be the remainder of the science telemetry, which is processed as it is played back. The L1 "Final" data set will replace the quick-look Part 2.

Level 2 data is calibrated data. Our experience suggests that it is more efficient to let the user generate the Level 2 data using standard software provided by the WISPR team as part of the Solarsoft library. Users are assured of having the latest calibration factors, and the operations team does not have to generate a new set of data every time calibrations are updated. A best and final Level 2 dataset will be provided when final calibrations are available, or after the end of the mission.

4.4.1 Data Archive

A complete archive (data products, metadata, planning documents, analysis software, etc.) will be maintained at NRL at least during the full mission lifetime. There will be a second copy of the complete archive, updated at least daily. The second copy may be at a TBD partner institution. WISPR data will be migrated to new storage hardware as part of the NRL Solar and Heliospheric Physics Branch long-term data maintenance plan. There is no plan to have the full data set on a removable storage media such as DVD.

In addition, the WISPR team will provide the final instrument calibration and a complete best and final Level-2 calibrated data set from the entire mission to an appropriate NASA archive at the end of Phase F or the end of the extended mission.

The WISPR data policy dictates completely open access to all data, including: Planning, Quick-look, and Final data products, the calibration data, and all procedures to calibrate and perform high-level processing of the data. NRL will maintain a web interface to a database of all science and housekeeping data that will permit users to search for data corresponding to time periods or events of interest using selected values from the image header, as well as to perform trend analysis of instrument housekeeping parameters such as temperatures and voltages. Validated science data will be distributed directly from NRL to requesters based on the results of a database query. Requests for larger amounts of data will be handled through the SPP Science Data Portal or the Virtual Solar Observatory (VSO).

4.4.2 Data Release Schedule

There will be two versions of WISPR processed science data: quick-look data produced immediately upon receipt of any image telemetry from the spacecraft (including a low-latency "planning" subset), and final data incorporating any telemetry packets that may be missing or corrupted in the quick-look telemetry and that are later recovered. (See Sect. 4.4.) Quicklook L1 data may be used for mission operations planning purposes and will be made public as soon as it is processed.

Final L1 data will replace the quicklook data and will be differentiated from the quick-look L1 data product in the FITS image header via the VERSION keyword. The Final L1 and resulting visualization data products will be (re-)generated after each orbit. These will be suitable for archiving and distribution. Both quick-look and final data will be processed in the same way and will have the same file formats.

4.4.3 Data Catalogues

The WISPR project will use an open source database program such as MYSQL, which is currently being used to manage the housekeeping and image header information on both SECCHI and LASCO. A web-based tool enables searches of the image header database with the ability to select FITS files for download using FTP to the user's computer. The table structures will be similar to the existing tables. For example, the existing IDL tools include the ability to extract any parameter(s) of interest and to generate plots against time or to correlate one parameter against another.

It is our intention that the FITS header will mirror the SPASE catalog. To the extent that the required keywords are known, they will be incorporated into the image FITS headers.

4.4.4 Documentation

Documentation necessary for data analysis and interpretation will be made available through the WISPR website. These will include

1. Instrument description.
2. Calibration and Validation methodology.
3. Validation through cross-calibration with other instruments or other assets (if applicable).
4. Dataset description including FITS header definition.
5. Meta-data products.

4.4.5 Processing and Analysis Tools

The radiometric calibration of the data will be performed using the pre-flight laboratory calibration data and calibration updates using observations of an ensemble of stable stars as used for SOHO/LASCO and STEREO/SECCHI. The calibration team monitors the detector telemetry and the images and provides periodic updates to the science calibration routines. IDL procedures will be provided in the Solarsoft library to convert the Level-1 FITS image files into higher-level calibrated data products. These procedures will permit the user to perform standard corrections such as removal of geometric distortion, vignetting and stray light, and photometric calibration, on-the-fly for the data of interest. All calibration data necessary for these corrections will be included as part of the Solarsoft distribution which is publicly available at http://sohowww.nascom.nasa.gov. This approach has been used successfully for both LASCO and SECCHI, and ensures that the user has access to the most up-to-date calibrations while avoiding repeated processing and redistribution of large amounts of data.

Software tools for common analysis tasks that are in use for LASCO, SECCHI, and SoloHI will be extended to incorporate WISPR data. These include image visualization, generation of movies, feature tracking, structure measurement, and combining datasets from multiple remote-sensing and *in-situ* instruments and spacecraft. Forward fitting of three-dimensional models to heliospheric features such as streamers and CMEs will also be provided in Solarsoft. NRL will work with the Community Coordinated Modeling Center (CCMC) at NASA Goddard Space Flight Center to produce appropriate heliospheric model calculations for comparison with the WISPR data for each Carrington rotation, as well as for selected events of interest. The results of these model calculations will be made publicly available on the WWW.

5 Summary

The Solar Probe Plus is NASA's most audacious robotic mission yet. Sending a probe to within a mere seven million kilometers from the surface of a star faces serious technological and environmental challenges but the scientific rewards will be boundless.

In the case of WISPR, the SPP orbit allows us to directly observe the internal structure of the corona with a greatly reduced interference from the F-corona, to make the first true tomographic maps of the 3D coronal density structure, to verify the existence of a dust ring close to the Sun and Vulcanoids within the Mercury orbit, to image structures at spatial scales close to the dissipation range, to capture the formation of shocks, to observe the final moments of sun-grazer comets and even, to image CMEs from the 'inside'. But all these are just educated guesses based on coronal imaging from 1 AU. The WISPR images probably hold many surprises and this makes SPP one of the most exciting space missions ever.

The WISPR program has successfully completed its preliminary design phase and is looking forward to the next and final review (Critical Design Review) scheduled for December 2014. We have no major concerns for the instrument at this point. The environmental challenges (stray light, dust impacts, radiation levels) have been addressed, the flight detectors are ready, the optical design is excellent, and the overall project is on schedule and within budget. We are all excited for the time when we will gaze at the first images from inside the Sun's atmosphere.

Acknowledgements This work is sponsored by the NASA LWS program through interagency agreement NNG11EK11I to NRL. The German contribution to WISPR is sponsored by the Deutsches Zentrum für Luft- und Raumfahrt (Grant No: FKZ 50OL1201). The Belgian contribution is sponsored by the Belgian Science Policy Office (BELSPO). The French contribution is sponsored by the Centre National d'Etudes Spatiales (CNES).

References

S.K. Antiochos et al., Structure and dynamics of the Sun's open magnetic field. Astrophys. J. **671**, 936 (2007)

S. Bale et al., The FIELDS investigation. Space Sci. Rev. (2015, this issue)

A. Bemborad et al., UVCS observation of sungrazer C/2001 C2: possible comet fragmentation and plasma-dust interactions. Astrophys. J. **620**, 523 (2005)

A. Bemborad et al., Low-frequency Lyα power spectra observed by UVCS in a polar coronal hole. Astrophys. J. **677**, L137 (2008)

J.W. Bieber et al., Spaceship Earth observations of the Easter 2001 solar particle event. Astrophys. J. **601**, L103 (2004)

J.E. Borovsky, Eddy viscosity and flow properties of the solar wind: Co-rotating interaction regions, coronal-mass-ejection sheaths, and solar-wind/magnetosphere coupling. Phys. Plasmas **13**(5), 056505 (2006)

J.E. Borovsky et al., Flux tube texture of the solar wind: Strands of the magnetic carpet at 1 AU? J. Geophys. Res. **113**(A8), A08110 (2008)

G.E. Brueckner, The Large Angle Spectroscopic Coronagraph (LASCO). Sol. Phys. **162**, 375 (1995)

R. Bruno, V. Carbone, The solar wind as a turbulence laboratory. Living Rev. Sol. Phys. **2** (2005)

P.J. Cargill, Coronal magnetism: difficulties and prospects. Space Sci. Rev. **144**, 413–421 (2009)

W.A. Coles, J.K. Harmon, Propagation observations of the solar wind near the Sun. Astrophys. J. **337**, 1023 (1989)

N.U. Crooker et al., Large-scale magnetic field inversions at sector boundaries. J. Geophys. Res. **109**(A3) A03108 (2004)

C.E. DeForest et al., Inbound waves in the solar corona: a direct indicator of Alfvén surface location. Astrophys. J. **787**, 124 (2014)

D. Durda et al., A new observational search for vulcanoids in SOHO/LASCO coronagraph images. Icarus **148**, 312 (2000)

G. Einaudi et al., Formation of the slow solar wind in a coronal streamer. J. Geophys. Res. **104**, 521 (1999)

G. Einaudi et al., Plasmoid formation and acceleration in the solar streamer belt. Astrophys. J. **633**, 474 (2001)

W.C. Feldman et al., Constraints on high-speed solar wind structure near its coronal base: a ULYSSES perspective. Astron. Astrophys. **316**, 355 (1996)

N. Fox et al., The solar probe plus mission. Space Sci. Rev. (2015, this issue)

N. Gopalswamy et al., Intensity variation of large solar energetic particle events associated with CMEs. J. Geophys. Res. **109**, A12105 (2004)

J.T. Gosling et al., Coronal streamers in the Solar Wind at 1 AU. J. Geophys. Res. **86**, 5438–5448 (1981)

J.T. Gosling et al., Observations of magnetic reconnection in the turbulent high-speed solar wind. Astrophys. J. **671**, L73 (2007)

S.R. Habbal et al., Origins of the slow and the ubiquitous fast solar wind. Astrophys. J. **489**, 103 (1997)

A. Hayes et al., Deriving the electron density of the solar corona from the inversion of total brightness measurements. Astrophys. J. **548**, 1081 (2001)

J.V. Hollweg, The solar wind: our current understanding and how we got here. J. Astrophys. Astron. **29**, 217 (2008)

A. Howard et al., The solar and heliospheric imager (Solohi) instrument for the solar orbiter mission. Proc. SPIE (2013, this issue)

R.A. Howard et al., Sun Earth Connection Coronal and Heliospheric Investigation (SECCHI). Space Sci. Rev. **136**, 67–115 (2008)

B.V. Jackson, C. Leinert, HELIOS images of Coronal Mass Ejections. JGR **90**, 10 (1985)

M. Jones et al., Imaging of a circumsolar dust ring near the orbit of venus. Science **342**, 6161 (2013)

S.W. Kahler, The correlation between solar energetic particle peak intensities and speeds of coronal mass ejections: Effects of ambient particle intensities and energy spectra. J. Geophys. Res. **106**, 20947 (2001)

S.W. Kahler, A. Vourlidas, Fast coronal mass ejection environments and the production of solar energetic particle events. J. Geophys. Res. **110**, A12S01 (2005)

S.W. Kahler, A. Vourlidas, A comparison of the intensities and energies of gradual solar energetic particle events with the dynamical properties of associated coronal mass ejections. Astrophys. J. **769**, 143 (2013)

M.J. Kaiser et al., The STEREO mission: an introduction. Space Sci. Rev. **136**, 5 (2008)

J. Kasper et al., The SWEAP investigation. Space Sci. Rev. (2015, this issue)

H. Kimura et al., Dust grains in the comae and tails of sungrazing comets: modeling of their mineralogical and morphological properties. Icarus **159**, 529 (2002)

M.M. Knight et al., Photometric study of the Kreutz comets observed by SOHO from 1996 to 2005. Astron. J. **193**, 926–949 (2010)

J.L. Kohl et al., The ultraviolet spectrometer for the solar and heliospheric observatory. Sol. Phys. **162**, 317 (1995)

C.M. Korendyke et al., Development of the solohi active pixel sensor. Proc. SPIE (2013, this issue)

J.M. Laming, Non-Wkb models of the first ionization potential effect: implications for solar coronal heating and the coronal helium and neon abundances. Astrophys. J. **695**(2), 954–969 (2009)

M.A. Lee, Acceleration of energetic particles on the Sun, in *The Heliosphere and in the Galaxy*, ed. by R.A. Mewaldt et al. AIP Conf. Ser., vol. 528 (AIP, Melville, 2000), p. 3

C. Leinert, B. Moster, Evidence for dust accumulation just outside the orbit of venus. Astron. Astrophys. **472**, 335 (2007)

C. Leinert et al., The zodiacal light from 1.0 to 0.3 AU as observed by the HELIOS space probes. Astron. Astrophys. **103**, 177 (1981)

C. Leinert et al., The 1997 reference of diffuse night sky brightness. Astron. Astrophys. Suppl. Ser. **127**, 1 (1998)

M.G. Linton et al., Patchy reconnection in a Y-type current sheet. Earth Planets Space **61**, 573 (2009)

I. Mann et al., Dust cloud near the Sun. Space Sci. Rev. **110**, 269 (2004)

E. Marsch, C.-Y. Tu, Spectral and spatial evolution of compressible turbulence in the inner solar wind. J. Geophys. Res. **95**, 11945 (1990)

G. Matthaeus, M.L. Goldstein, Low-frequency $1/f$ noise in the interplanetary magnetic field. Phys. Rev. Lett. **57**, 495 (1986)

D. McComas et al., The ISIS investigation. Space Sci. Rev. (2015, this issue)

D.S. Mehoke et al., A review of the solar probe plus dust protection approach, in *Aerospace Conf., IEEE* (2012), pp. 1–13. doi:10.1109/AERO.2012.6187076

W.J. Merline, A program to search for vulcanoids from MESSENGER. Bull. Am. Astron. Soc. **40**, 491 (2008)

R.A. Mewaldt et al., How efficient are coronal mass ejections at accelerating solar energetic particles?, in *Proc. of Solar Wind* (2005), p. 11

D. Müller, R.G. Marsden, O.C. St. Cyr, H.R. Gilbert, Solar orbiter—exploring the Sun-heliosphere connection. Sol. Phys. **285**, 25–70 (2013)

E.N. Parker, Cosmic ray modulation by solar wind. Phys. Rev. **110**(6), 1445–1449 (1958)

B.R. Ragot, S.W. Kahler, Interactions of dust grains with coronal mass ejections and solar cycle variations of the F-coronal brightness. Astrophys. J. **594**, 1049–1059 (2003)

A.F. Rappazzo et al., Diamagnetic and expansion effects on the observable properties of slow solar wind in an coronal streamer. Astrophys. J. **633**, 474–488 (2005)

D.V. Reames, Particle acceleration at the Sun and in the heliosphere. Space Sci. Rev. **90**, 413 (1999)

A.P. Rouillard et al., First imaging of corotating interaction regions using the STEREO spacecraft. Geophys. Res. Lett. **35**(10), L10110 (2008)

A.P. Rouillard et al., A multispacecraft analysis of a small-scale transient entrained by solar wind streams. Sol. Phys. **256**, 307 (2009)

H.N. Russell, On meteoric matter near the stars. Astrophys. J. **69**, 49 (1929)

R. Schwenn, Direct observation of the latitudinal extent of a high-speed stream in the solar wind. J. Geophys. Res. **83**, 1011 (1978)

Z. Sekanina, Kreutz sungrazers: the ultimate case of cometary fragmentation and disintegration? Proc. Astron. Inst. Acad. Sci. Czech Repub. **89**, 78 (2001)

N.R. Sheeley Jr., Y.-M. Wang, Coronal inflows and sector magnetism. Astrophys. J. **562**, L107 (2001)

N.R. Sheeley Jr., Y.-M. Wang, Characteristics of coronal inflows. Astrophys. J. **579**, 874 (2002)

N.R. Sheeley Jr. et al., Measurements of flow speeds in the corona between 2 and 30 R_S. Astrophys. J. **484**, 472 (1997)

N.R. Sheeley Jr. et al., Heliospheric images of the solar wind at Earth. Astrophys. J. **675**, 853 (2008)

C.W. Snyder, M. Neugebauer, U.R. Rao, The solar wind velocity and its correlation with cosmic-ray variations and with solar and geomagnetic activitiy. J. Geophys. Res. **68**, 6361 (1963)

D.G. Socker et al., The NASA Solar Terrestrial Relations Observatory (STEREO) mission heliospheric imager. Proc. SPIE **4139**, 284–293 (2000)

A.J. Steffl et al., A search for vulcanoids with the STEREO heliospheric imager. Icarus **223**, 48 (2013)

A.F. Thernisien, R.A. Howard, Electron density modeling of a streamer using LASCO data of 2004 January and February. Astrophys. J. **642**, 523 (2006)

A.F. Thernisien et al., Photometric calibration of the Lasco-C3 coronagraph using stars. Sol. Phys. **233**, 155 (2006)

A.F. Thernisien et al., Forward modelling of coronal mass ejections using STEREO-SECCHI data. Sol. Phys. **256**, 111 (2009)

A. Tylka, Shock geometry, seed populations, and the origin of variable elemental composition at high energies in large gradual solar particle events. Astrophys. J. **625**, 474 (2005)

N.M. Viall et al., Are periodic solar wind number density structures formed in the solar corona? Geophys. Res. Lett. **36**(23), L23102 (2009)

N.M. Viall et al., Are periodic solar wind number density structures formed in the solar corona? Geophys. Res. Lett. **36**(23), 23102 (2009)

N.M. Viall et al., Examining periodic solar-wind density structures observed in the SECCHI heliospheric imagers. Sol. Phys. **267**, 175 (2010)

A. Vourlidas et al., On the interpretation of Thomson scattering brightness from vantage points within 1 AU: implications for heliospheric imaging from solar orbiter and solar probe plus. Astrophys. J. (2015, submitted)

A. Vourlidas, R.A. Howard, The proper treatment of coronal mass ejection brightness: a new methodology and implications for observations. Astrophys. J. **642**, 1216 (2006)

A. Vourlidas, V. Ontiveros, A review of coronagraphic observations of shocks driven by coronal mass ejections, in shock waves in space and astrophysical environments, in *18th Annual Int. Astroph. Conf.* AIP Conf. Proc., vol. 1183 (2009), p. 139

A. Vourlidas, P. Riley, Direct imaging of the heliospheric plasma sheet from the SECCHI telescopes on the STEREO mission. Eos Trans. AGU **88**(52) (2007). Abstract SH21A-0283

Y.-M. Wang, N.R. Sheeley Jr., Solar wind speed and coronal flux-tube expansion. Astrophys. J. **355**, 726 (1990)

Y.-M. Wang, N.R. Sheeley Jr., Observations of flux rope formation in the outer corona. Astrophys. J. **644**, 638 (2006)

Y.-M. Wang et al., Coronagraph observations of inflows during high solar activity. Geophys. Res. Lett. **26**, 1203 (1999a)

Y.-M. Wang et al., Streamer disconnection events observed with the LASCO coronagraph. Geophys. Res. Lett. **26**, 1349 (1999b)

Y.-M. Wang, N.R. Sheeley, N.B. Rich, Coronal pseudostreamers. Astrophys. J. **658**, 1340–1348 (2007)

R. Woo, J.M. Martin, Source regions of the slow solar wind. Geophys. Res. Lett. **24**, 2535 (1997)

T.V. Zaqarshvili et al., Twisted magnetic flux tubes in the solar wind. Astrophys. J. Lett. **783**, L19 (2014)

T.H. Zurbuchen et al., The solar wind composition throughout the solar cycle: a continuum of dynamic states. Geophys. Res. Lett. **29**(9), 1352 (2002). 66-1